Chapter 2

Molecular Beam Epitaxy

The two most widely used methods for semiconductor heterostructure growth are metal organic chemical vapor deposition (MOCVD) and molecular beam epitaxy (MBE). MOCVD is a vapor phase deposition process involving metal alkyls and hydrides, and is typically conducted at low or atmospheric pressure [1]. Although the MOCVD technique has been successfully used for the growth of high quality heterostructure devices such as quantum well lasers and heterojunction field effect transistors, it has not fared as well for tunneling based structures such as DBRTDs. In fact, the highest peak-to-valley current ratio (PVCR) reported for MOCVD grown AlGaAs/GaAs DBRTDs is 3.0 with a peak current density, J_p, of 7 kA/cm^2 [2]. In contrast MBE grown AlGaAs/GaAs DBRTDs with similar dimensions have achieved PVCR as high as 3.9 with a J_p of 7 kA/cm^2 [3]. The better performance is primarily due to the superior interface quality of MBE grown devices and to the accumulation of impurities at the heterointerface of MOCVD grown DBRTD structures [4]. Furthermore, MOCVD grown DBRTDs with peak current densities higher than 10 kA/cm^2, have not been reported. For very high speed applications, current densities on the order of 100 kA/cm^2 are required, necessitating the use of extremely thin layers (six monolayers or less). Such thin layers with abrupt interfaces are difficult to grow reproducibly by MOCVD. For reasons that will become apparent, MBE is the desired process for the reproducible growth of tunneling-based devices.

In this chapter, the MBE growth technique and the use of reflection high energy electron diffraction (RHEED) in the optimization of growth conditions for high performance DBRTDs will be discussed. Further, the MBE growth and materials characterization of InAlGaAs/InP structures will be discussed.

2.1 Introduction to the Varian Gen II MBE system

MBE is essentially an evaporation technique conducted in an ultrahigh vacuum (UHV) environment [5,6]. A schematic diagram of this technique is given in Fig. 2.1. The UHV environs serves several purposes. First, the molecular beam is kept collimated since the mean free path is much greater than the chamber dimensions. Second, the background impurity concentration is kept very low (partial pressures < 10^{-12} Torr). Third, surface analysis tools such as RHEED can be used as an in-situ monitor of the growth kinetics.

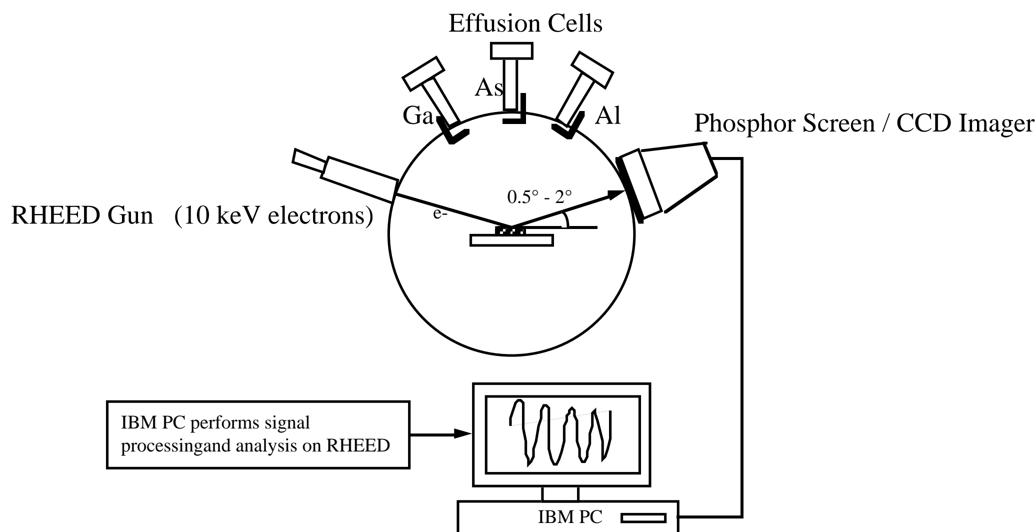

Fig. 2.1 Schematic diagram of the Varian GENII growth chamber showing the effusion cells and RHEED system geometry.

Each effusion cell or furnace contains an elemental material of very high purity. The effusion cells are heated to a high enough vapor pressure such that there is a "molecular beam" impinging on to a heated substrate. The deposition or growth rate is very slow, typically one monolayer of GaAs (2.83Å) per second. Thus, with shutters placed in front of the furnaces, one can interrupt the " molecular beam" in a

fraction of a second, thereby affording monolayer control over both doping and composition. Therefore, with MBE, in addition to growing "bandgap engineered" devices one can also study and optimize the growth process.

The University of Texas Varian GEN II MBE system consists of three interconnected vacuum chambers: the load lock chamber, the prep chamber, and the growth chamber. Samples are introduced into the system through the load lock where they are initially outgassed to remove any volatile contaminants. Then, the samples are transferred from the load lock to the prep chamber via a magnetically coupled transfer rod. They are again outgassed to ensure removal of any remaining volatile contaminants and then transported, via another transfer rod, to the growth chamber for epitaxial growth. The growth chamber contains a sample manipulator that can be rotated from the docking position (where the sample faces the prep chamber), 180° to the growth position (sample faces the effusion cells). The sample manipulator houses a substrate heater on one side and an ionization gauge on the opposite side. This ionization gauge, called the beam equivalent pressure (BEP) gauge, when facing the effusion cells, measures the BEP flux emanating from the cells. The BEP is proportional to the flux of evaporated species that would be impinging on the sample if it were in the growth position. The substrate heater also has the capability of continuous azimuthal rotation of rates up to 150 revolutions per minute. Hence, the sample manipulator is known as the Continuously Azimuthal Rotation (CAR) and is one of the most critical components in the system and unfortunately, failure prone. The background pressure in the chamber is monitored by a second ionization gauge located near the prep-to-growth chamber gate valve. There are an assortment of vacuum pumps for each chamber. The load lock has a 50 liters per sec (lps) Balzers turbo-molecular pump and a 60 lps ion pump, which maintain the load lock at approximately 10^{-7} Torr. There are also three VacSorb adsorption pumps that are used to evacuate the load lock from atmospheric pressure to the cross-over pressure of the turbo-molecular pump (~ 60 mTorr). The prep chamber is pumped by a 200 lps ion pump that maintains the chamber at approximately 10^{-9} Torr. There is also a

titanium sublimation pump in the prep chamber which is only operated when the chamber has been recently exposed to air. The growth chamber is pumped on by two 3000 lps CVI closed cycle cryo-pumps. The top half of the growth chamber is enclosed in a liquid nitrogen cryo-shroud that, when combined with the cryo-pumps, provides an UHV environment of less than 2×10^{-10} Torr. The growth chamber vacuum integrity is monitored by a quadrapole mass spectrometer that measures the relative concentrations of various molecular species present in the residual background.

The Varian GEN II has eight effusion cells: one each of aluminum, indium, silicon, beryllium, and two each of gallium and arsenic. The gallium and arsenic sources used in this work are designated Ga1 and As1. The As1 cell is a patented, dual zone design consisting of a one kilogram capacity sublimator and a cracking section [7]. The typical arsenic sublimator charge is 400 grams. The sublimator is heated to approximately 350°C and the arsenic sublimes as As_4. The As_4 molecules are then cracked into As_2 and the cracking temperature, typically 650°C, is set to achieve both high cracking efficiency (greater than 80%) and good material properties. Once the cracker temperature is set, the sublimator temperature is raised to the desired temperature and allowed to stabilize, a procedure requiring four to six hours due to the large thermal mass of the arsenic chunks. More recently, the As1 source was modified to incorporate a needle valve between the sublimator and the cracker tube [8]. In this arrangement, the sublimator temperature is maintained at 350°C and the BEP with the valve totally open is typically about 5×10^{-5} Torr. At the beginning of the growth cycle, the user adjusts the valve position to obtain the desired arsenic flux. Then, at the end of the growth cycle, the valve is closed to conserve the arsenic charge. In practice, the valve is not closed all the way but to a point such that the arsenic BEP is less than 10^{-7} Torr. The valved cracker/sublimator arrangement has proven to be very convenient since one no longer has to wait several hours for the arsenic flux to stabilize before one can begin to perform growth rate calibrations.

2.2 MBE Growth Kinetics

MBE growth is a non-equilibrium process that involves (a) adsorption of constituent atoms and molecules, (b) surface migration to appropriate lattice sites, and (c) incorporation into the growing film [9]. The established model for MBE growth is based on the pioneering work of Foxon and Joyce and is summarized in Fig. 2.2. GaAs is generally grown by MBE through the dissociative chemisorption of either As_2 or As_4 with gallium atoms. As discussed earlier, elemental arsenic sublimates in the tetramer form but can be cracked to As_2 by thermally dissociation. For the case of a Ga atom and an As_2 molecule, the growth reaction is due to dissociative chemisorption of As_2 molecules on Ga atoms. The sticking coefficient of As_2 is such that any excess arsenic is desorbed, leading to stochiometric GaAs growth. The case of a Ga atom and an As_4 molecule is slightly more involved since the sticking coefficient of As_4 is half that of As_2. Here, pairs of As_4 molecules react on adjacent Ga sites such that four arsenic atoms are incorporated into the GaAs lattice and the remaining four arsenic atoms desorb as an As_4 molecule. It is preferable to use As_2 rather than As_4 since its much higher sticking coefficient will reduce source depletion effects and therefore increase the system up-time.

As one can expect with a non-equilibrium and rate limited process, MBE growth is very temperature dependent. At very low growth temperatures, the cation (group III adatom) surface mobility is severely degraded, resulting in a rough surface or even non-crystalline growth. At very high temperatures, on the other hand, adatom re-evaporation will lead to surface roughening and interlayer mixing. For the growth of the InAlGaAs devices described in this work, the growth temperatures range from 500°C to 600°C. At these temperatures, since there is significant re-evaporation of arsenic, the growth is conducted in an arsenic overpressure. Consequently, the growth rate is determined by the group III atomic flux since the arsenic can only be adsorbed and incorporated into the lattice if there are free group III adatoms available for bonding.

As a note, recently very low temperature grown (~ 200°C) LT-GaAs followed with a high temperature (~ 600°C) anneal has shown to have favorable properties for high speed device applications [[10]]. In fact, in Chapter 5 we shall discuss the electrical characteristics of LT-GaAs based varactor diodes.

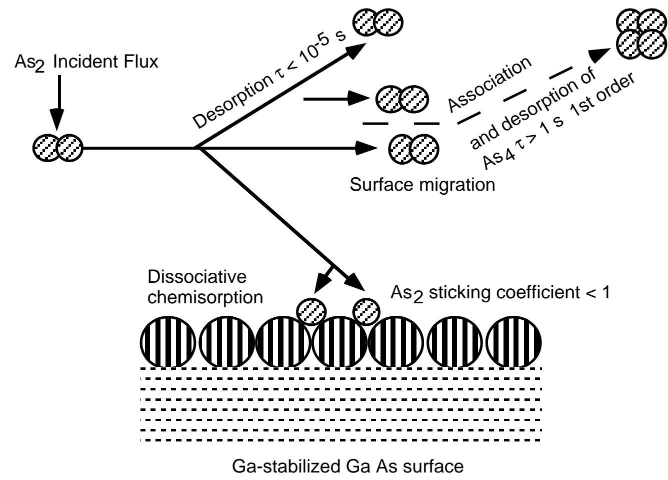

(a)

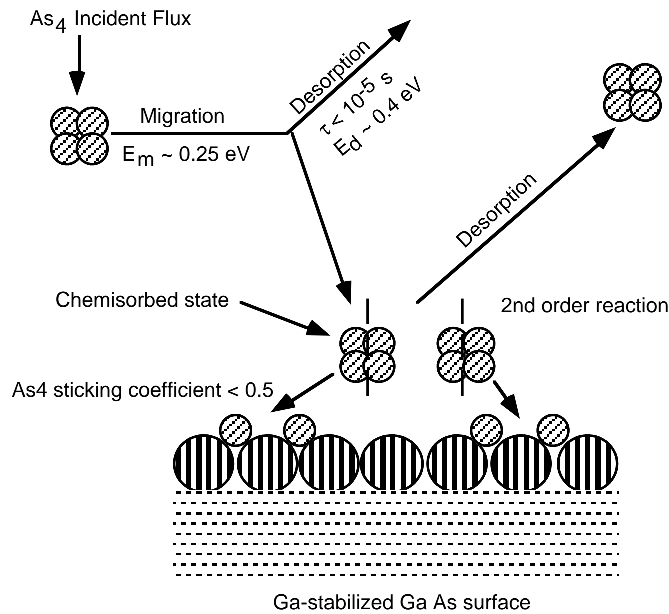

(b)

Fig. 2.2 (a) Model for the growth of GaAs from Ga and As2. (b) Model for the growth of GaAs from Ga and As4. Adapted from E. H. C. Parker, " Technology and Physics of Molecular Beam Epitaxy," Plenum, p. 49, 1985.

2.3 Reflection High Energy Electron Diffraction (RHEED)

Since MBE is an UHV process, powerful surface analysis tools such as RHEED can be utilized as in-situ growth monitors. The growth condition optimization experiments and growth rate calibrations for the InAlGaAs growth described later in this chapter were done with RHEED. A schematic of the RHEED system on our Varian GEN II MBE system is given in Fig. 2.1. In RHEED, high energy electrons (~ 10 KeV) impinge on the substrate at a glancing angle (0.5° - 2°). The diffraction pattern due to the shallow angle reflection is imaged on a phosphor screen and the pattern is collected by a CCD imaging system. Since the angle of incidence is very small, the kinetic energy of the impinging electrons normal to the surface is very small and they essentially sample the surface only. The diffraction images provide information on the surface reconstructions present and the surface smoothness on an atomic scale. Once the diffraction pattern is stored in the computer, the pattern is processed to extract parameters of interest. In our system we monitor the RHEED beam intensity only over a small square shaped area since we are only interested in the specular spot intensity.

The utility of RHEED can be appreciated by considering the Ewald construction for the high energy electrons and the surface. For an idealized surface, the reciprocal lattice is composed of infinite rods intersecting the plane at the lattice points normal to the surface . The intersection of the surface reciprocal lattice and the electron's Ewald sphere results in a diffraction pattern consisting of streaks as shown in Fig. 2.3. These patterns are observed at typical MBE growth temperatures (500°C to 600°C). Following Wood's convention, the surface structure denoted by (*m x n*) means that the surface layer, due to the reconstruction, has an unit cell which is (*m x n*) times larger than the underlying cell [11]. During growth the surface is arsenic stabilized and the RHEED pattern is denoted as (2 x 4) which means that the reconstructed surface manifests itself in the RHEED

pattern as 1/2 and 1/4 order streaks in the (110) and ($\underline{1}$10) azimuths, respectively. These fractional order streaks that appear as lines between the bulk surface streaks arise from surface adatoms reorganizing to energetically favorable configurations.

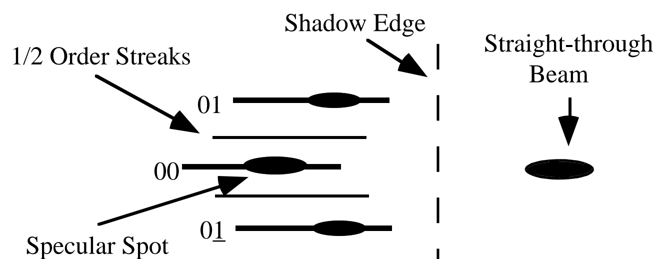

(110) Azimuth - 2 x 4 As stable Surface

(a)

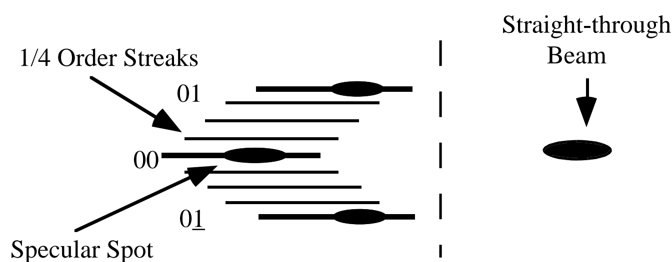

($\underline{1}$10) Azimuth - 2 x 4 As stable Surface

(b)

Fig. 2.3 Depiction of (a) As-stable (2 x 4) RHEED pattern in (110) direction (b) As-stable (2 x 4) RHEED pattern in ($\underline{1}$10) direction or 90° off. The straight through beam and the shadow edge are also shown with respect to the pattern.

In addition to monitoring surface reconstructions, one can also measure the growth rate with RHEED by monitoring the temporal oscillations of the specular spot beam intensity as shown in Fig. 2.4.

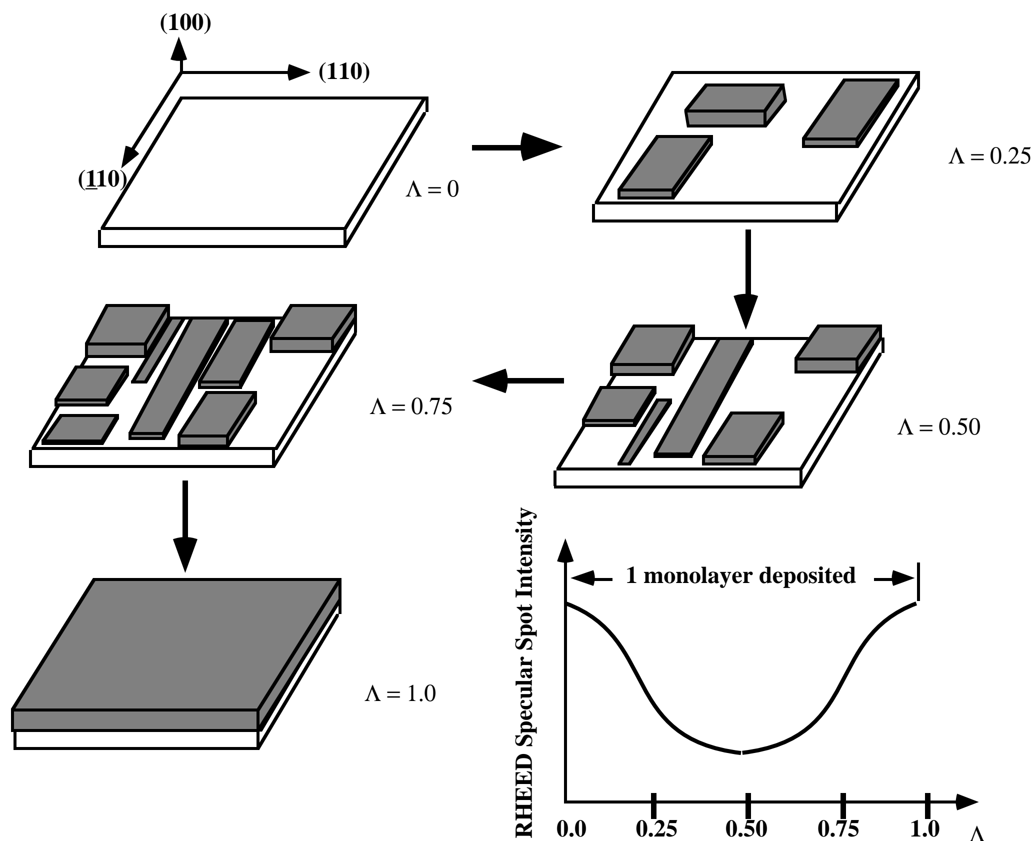

Fig. 2.4 Relationship between RHEED specular spot intensity and monolayer deposition. λ is the surface coverage. The intensity oscillates with a period determined by the deposition rate. The intensity at 50% surface coverage is at the minimum due to the maximum scattering at this point.

It is instructive to assume that the electron gun angle is set at the angle that gives the maximum specular spot intensity and that the surface is perfectly smooth. As a new monolayer is deposited, the surface becomes rougher and the electron beam is scattered which reduces the reflected beam intensity. When half of the surface is covered, the electron beam experiences maximum roughness and the intensity is at a minimum. Upon completion of the new monolayer the intensity will again rise to its maximum value. In practice, these intensity oscillations are

damped since the growth front is distributed over terraces and islands and not a perfectly flat surface Further, the damping of the oscillations is dependent on growth and diffraction conditions [12]. However, if the growth parameters and diffraction conditions are optimized in a reproducible manner as will be shown in the next section, information extracted from the intensity oscillations can be used for reliable growth rate measurements.

Assuming that reliable measurements are made, one can plot the oscillations as a function of time and determine the growth rate, R (Å/sec), as:

$$R = \frac{L}{T_{osc}} \tag{2.1}$$

where L is the thickness of one monolayer (2.83Å for GaAs) and T_{OSC} is the period of one complete intensity oscillation. One can also measure the alloy composition by this technique. For example, when growing $Al_xGa_{1-x}As$, x is given by:

$$x = \frac{R(AlAs)}{R(AlAs) + R(GaAs)} \tag{2.2}$$

where R(AlAs) and R(GaAs) are the growth rates of the binary compounds of AlAs and GaAs, respectively. This procedure can be easily extended to the lattice-matched InAlGaAs material system as will be shown later in this chapter for calibrating alloy compositions and growth rates.

In addition to calibrating growth rates and alloy compositions, RHEED is also used to optimize the arsenic overpressure. From the discussion on MBE growth kinetics and RHEED, it is clear that the arsenic overpressure strongly influences the growth front. A 2-D growth front is achieved if the metal cations can migrate to a step edge before they are incorporated into the crystal surface. This migration time depends on the amount of excess arsenic present at the surface and whether it is in dimer or tetramer form. It follows then that the arsenic

overpressure should be reduced to improve the adatom mobility. However, there is a lower limit on the arsenic flux. If the cation flux is greater than the arsenic flux, the surface will become metal rich and metal droplets will form on the surface. These droplets will roughen the surface and non-stochiometric growth will occur [[13]]. But too high an overpressure will result in reduced adatom mobility and rough interfaces during the growth of heterostructures. Therefore, there is an arsenic overpressure "window" that will provide optimum growth.

The actual values reported in the literature for typical arsenic overpressures vary considerably, by a factor of two. This is due to the common practice in the MBE community, when describing the arsenic overpressure, to quote the ratio of the arsenic flux to the metal cation flux. This ratio is not a very useful quantity since it is a function of several parameters: chamber geometry, ion gauge sensitivity, substrate temperature, and cation characteristics. A more appropriate quantity is the incorporation coefficient, I_c, which was introduced by Lewis et al.. [[14]]. It is a measure of the arsenic that is actually incorporated into the crystal and does not include the arsenic lost during the dissociation of incoming arsenic molecules or that which re-evaporates from the surface.

The incorporation coefficient for a given substrate temperature, arsenic overpressure, and growth rate is measured as follows. Taking the case of GaAs growth, one begins by allowing the initial growth surface to be arsenic stable with a (2 x 4) RHEED pattern. Then GaAs growth proceeds by opening the group III shutter (gallium) for ten seconds. Then the arsenic cell is shuttered off for a time period, T1 (typically five to 10 seconds). During this interval, the RHEED patterns converts to a (4 x 2) state, that of a metal stable surface. Then after the time interval T1, the arsenic shutter is re-opened and the RHEED pattern is monitored as the pattern changes from the (4 x 2) to the arsenic stable, (2 x 4) state. The time required for this conversion is T2. I_c is then defined as:

$$I_c = \frac{T1 + T2}{T2} = 1 + \frac{T1}{T2} \qquad (2.3)$$

The time T2 is inversely proportional to the excess arsenic flux at the surface since it is the time required for the excess arsenic atoms to bond with the metal cations to create an arsenic stable surface. Therefore, an I_c much greater than one indicates that the overpressure is too high. Such a high overpressure will reduce the cation surface migration length and lead to a rougher growth front. However, if I_c is close to one, signifying insufficient arsenic, metallic droplets will form and result in non-stochiometric growth. We have determined that an I_c between 1.5 and 1.7 for a GaAs growth rate of 1.0 ML/sec at 600°C results in sustained RHEED oscillations and good material properties.

2.4 Optimization of Growth Conditions for DBRTDs

To optimize the performance of DBRTDs, one can vary both structural and growth parameters. The structural parameters (layer dimensions and doping concentrations) are determined by the device application at hand. For microwave oscillator applications, as will be discussed in the next chapter, it is essential that the DBRTDs be high current density devices with low peak voltages. Such an application requires extremely thin barrier layers grown with a very high degree of reproducibility.

Further, it is important to have a "baseline" device whose characteristics are well understood and repeatable. Such a structure would allow rapid qualification of the MBE growth, device processing, and electrical testing. Moreover, the baseline device would function as a template for future device development whose structural parameters would be modifications of the baseline parameters. The following discussion will be confined to the AlAs/GaAs material system but the growth optimization considerations are similar for the InAlGaAs/InP material system, which will be covered later.

The layer schematic of our baseline device is given in Fig. 2.5. The layer dimensions and doping concentrations are based on previous work and analysis of the literature [[15]]. Once the structural parameters are determined, optimization of the growth conditions can begin.

Layer	Material
5000 Å n+ (5.0×10^{18} cm^{-3})	GaAs
100 Å n (5.0×10^{17} cm^{-3})	GaAs
100 Å n - (5.0×10^{16} cm^{-3})	GaAs
50 Å Undoped	GaAs
17 Å Undoped	AlAs
50 Å Undoped	GaAs
17 Å Undoped	AlAs
50 Å Undoped	GaAs
100 Å n - (5.0×10^{16} cm^{-3})	GaAs
100 Å n (5.0×10^{17} cm^{-3})	GaAs
5000 Å n+ (5.0×10^{18} cm^{-3})	GaAs
n+ GaAs Substrate	

Fig. 2.5 Layer Schematic of Baseline DBRTD. The quantum well consists of 50Å GaAs well and 17Å AlAs barriers. These layers are between a three step dopant transition region consisting of 100Å n-type (5×10^{17} cm-3) GaAs, 100Å n-type (5×10^{16} cm-3) GaAs, and finally 50Å of nominally undoped GaAs. Heavily doped (5×10^{18} cm^{-3}) layers serve as contact electrodes.

For a given material system, there are basically four parameters that need to be optimized: substrate temperature, growth rates, arsenic overpressure, and growth interruption time at an heterointerface. The substrate temperature is strongly influenced by the desorption characteristics of the group III constituents, in particular, by the weaker bond energy cation. The temperature chosen should let the adsorbed cations be energetic enough to migrate on the surface to a step edge but not too high that they begin to desorb. Typical substrate temperatures for AlGaAs growth vary from 560°C to 640°C [[16]]. For AlAs/GaAs growth, we have chosen a growth temperature of 600°C for several reasons that are outlined below. The RHEED growth rate calibrations are performed at 600°C since sustained intensity calibrations are easily obtained at this temperature. For the growth rate calibrations to be relevant, it is desirable that the growth temperature during device growth and growth rate calibration be identical, or at least similar. Furthermore, Campbell et. al. have shown that the deep level trap density in DBRTDs was reduced as the growth temperature was increased from 550°C to 650°C [[17]]. The motivation for their study was to examine the then commonly held belief in the DBRTD community that growth temperatures no higher than 560°C were required to prevent dopant migration into the quantum well and, consequently, to observe room temperature NDR. The results showed that the PVCR is not strongly affected by the increased growth temperature. Although, the devices studied in this paper were not state-of-the-art with respect to their PVCR, the study's conclusions are still valid. Cheng *et al.* have investigated AlAs/GaAs DBRTDs grown at 600°C where the AlAs barriers were doped [[18]]. Their findings indicate that the PVCR is not significantly affected by doping the barrier and therefore, silicon dopant diffusion does not appear to be an issue at this temperature.

The choice of growth rate depends on the substrate temperature and, to a large extent, on the thickness of the layer to be grown. For example, the heavily doped, 0.5 μm thick buffer and contact layers of the baseline DBRTD are typically grown at 1 monolayer (ML)/sec to reduce the growth time. On the other hand, when growing the extremely thin quantum well and barriers, the growth rate is

reduced so as to have more control over the layer thickness and interface sharpness. There is a trade-off, however, in that the background impurity concentration flux impinging on the substrate is independent of the growth rate. Therefore, as the growth rate is reduced a higher proportion of impurities are incorporated into the layer. For the growth of the surrounding cladding layers and the quantum well, we have chosen a growth rate of 0.4 ML/sec and 0.3 ML/sec for GaAs and AlAs, respectively. Since the barrier thickness of the baseline DBRTD is 17Å or 6 ML thick, the critical importance of a reproducible and accurate growth rate is readily appreciated. In fact, a monolayer variation in the barrier or well thickness can result in an order of magnitude variation in the current versus voltage (I-V) characteristics. It is clear at this point that MBE is ideally suited for DBRTD growth due to its precise control of layer thicknesses and in-situ monitoring capability.

The growth rate, as discussed earlier, is measured by monitoring the temporal oscillation of the specular spot intensity as shown in Fig. 2.4. Once the intensity oscillation data is acquired and stored in the PC, signal processing is performed on the data set to extract a growth rate. Presently, the growth rate extraction program, GRATE, returns values calculated by three techniques: auto correlation, padded FFT, and truncated FFT [19]. The first period of oscillation data is removed since the first oscillation can be dependent on the starting surface and diffraction conditions and not reflect the actual growth rate [20]. The auto correlation technique involves calculating the growth period as the average time between local maxima in the auto correlation function. The FFT techniques involve padding the data set with zeroes or truncating it to satisfy the FFT routine's requirement that the data set contain 2^n values, where n is an integer. A growth rate is obtained by transforming the data into the frequency domain and solving for the centroid of the peak. Confidence in a growth rate measurement is achieved when the values extracted through the three techniques vary by no more than two percent. A growth rate is considered calibrated when at least three high confidence measurements with a standard deviation of less than two percent are obtained.

Since flux non-uniformities are quite pronounced in our system, growth rates can vary by as much as twenty percent from the center to the edge of a two-inch diameter substrate. Therefore, a small (5 mm square) sample is used for the RHEED calibrations to reduce this non-uniformity problem. The flux non-uniformity is not really an issue during device growth since the samples are typically no larger than one square inch and are mounted on the center of the molybdenum block. Although we have not studied the effect of flux variation on DBRTD performance, we have not seen any significant difference (more than twenty percent variation) in electrical characteristics between devices at the edge and center of the wafer.

Once the substrate temperature and growth rates have been established, the optimum arsenic overpressure is easily determined through the incorporation ratio measurement discussed earlier. During the course of much of this work, the arsenic flux could not be rapidly varied through computer control . Therefore, the arsenic flux could not be optimized for each individual layer. Consequently, the flux was optimized for the highest growth rate used, 1 ML/sec, as this required the highest arsenic overpressure. For an AlAs/GaAs device growth this resulted in an arsenic BEP of 9×10^{-6} Torr with an incorporation ratio of 1.6 at a GaAs growth rate of 1 ML/sec and a substrate temperature of 600°C. Since the overpressure is not changed throughout the device growth, the incorporation ratio increases to approximately 3.2 during the slower deposition rate for the quantum well. Although this is not an optimum overpressure for the growth of the quantum well, the DBRTDs do not seem to suffer as evidenced by their state-of-the-art electrical characteristics [[21]].

The fourth parameter that can be optimized is the duration of a growth interrupt at a heterointerface. By growth interruption, we mean ceasing growth by closing the group III shutters with the arsenic shutter open and allowing the sample to anneal at the growth temperature.

Since the properties of DBRTDs depend on the quantum mechanical interaction of electrons at heterointerfaces, the microstructure of the interfaces is of great importance. Ideally, the interfaces should be atomically smooth across the whole device active area. In reality, of course, due to the stochastic nature of MBE growth, the growth front is distributed over several monolayers and consists of islands and terraces. A growth interrupt, in principle, allows the islands and terraces to coalesce and preserve the two-dimensionality of the growth front [[22]].

There is a vast body of literature on the effects of growth interruption on heterostructures. These studies can be divided into three areas: RHEED dynamics, luminescence techniques, and device characterization. RHEED has been used extensively to study interface formation and growth interruption effects during heterostructure growth. It is well established that the specular spot intensity is a measure of the two-dimensionality or smoothness of the growth front. Furthermore, the damping of the intensity oscillations to a steady state value results from reaching a steady-state terrace width distribution and the growth mode changing from two-dimensional to step propagation. A growth interruption allows surface cations sufficient time to migrate to terrace edges and kink sites. Since this increases the average terrace width or reduces step density, the surface smoothens and hence recovers the specular spot intensity to its starting value [[23]]. It should be pointed out that surface smoothening is temperature dependent as the adatom migration process is thermally driven.

Photoluminescence (PL) and photoluminescence excitation (PLE) spectroscopy of quantum wells is the second technique used to study growth interruption effects on interface quality. In high quality quantum wells, the exciton luminescence is the dominant transition and the quantum well interface quality is compared to the exciton diameter (approximately 200Å). Here, interface roughness is treated as lateral variations in the quantum well width. The interface morphology can be divided into three regimes with respect to the exciton diameter: smooth, rough, and pseudo-smooth . In the smooth regime, the average island size

is much larger than the exciton diameter and the PL spectra consists of narrow linewidth transitions. In the rough regime, the exciton diameter is comparable to the island size and the exciton samples several different well widths. Such a superposition of narrow linewidth transitions results in a broad PL peak. In the intermediate case of the pseudo-smooth regime, the mean island size or step density is much smaller than the exciton diameter and the interface is said to exhibit "microroughness" Here the excitons experience an average potential which is quite uniform over the exciton diameter. The PL transitions, in the pseudo-smooth regime, exhibit narrow linewidths but the transition energies differ from that of integer monolayer width quantum wells.

Tanaka and Sakaki have performed thorough investigations on the effects of growth interruption on interface roughness of $Al_xGa_{1-x}As$/GaAs quantum wells [[24]]. They measured quantum well PL linewidths for uninterrupted and interrupted samples where the aluminum mole fraction, x, was varied from x= 0.2 to 1. They observed that for quantum wells with x> 0.5, the interface roughness of the top (AlGaAs on GaAs) interface is significantly reduced with a growth interruption but the bottom (GaAs on AlGaAs) interface remains unchanged and acts as a pseudo-smooth interface. For QW's with x< 0.3, on the other hand, a growth interruption smoothens both interfaces. These observations are explained by the fact that the Ga adatom diffusion length is considerably larger than the Al adatom diffusion length [[25]]. Therefore, during the interrupt, the Ga atoms will migrate further than the Al atoms to terrace edges and kink sites. The Al atoms, due to their shorter diffusion length and higher bond energy, will tend to incorporate readily into the growing film. So, for high aluminum mole fraction layers, the microroughness is relatively independent of the interrupt duration. It is, however, a function of the substrate temperature since the migration length is dependent on the adatom thermal energy [[26]].

The information gained from the above studies, although relevant, can not be directly applied to DBRTDs. The RHEED and PL experiments, in particular,

examined growth interrupt effects on quantum wells, where there are only two relevant hetero-interfaces. DBRTDs, in contrast, have four relevant hetero-interfaces: the AlGaAs/GaAs interfaces on both sides of the barriers. This distinction is due to the fact that DBRTDs are perpendicular transport devices whose operation is critically dependent on all the hetero-interfaces. This is not the case for parallel transport devices, such as high electron mobility transistors. In fact, growth interruptions have been shown to be highly beneficial in obtaining HEMT structures with electron mobilities as high as 10^7 cm^2/V-s [27]. Therefore, to further improve DBRTD performance it is important that the effects of growth interruption on DBRTD characteristics be studied.

To date, only one study on the effects of growth interruption on DBRTDs was reported by Gueret et al. at IBM at Zurich [28]. They presented data on AlGaAs/GaAs DBRTDs with very low barrier heights (120 meV) and very thick barriers (275Å). The measurements were conducted at 4K. Three samples were grown with interruptions of 0 s, 10 s, and 30 s at the inverted (GaAs grown on AlGaAs) interface. They observed that the peak current increased with the interrupt time while the valley current remained relatively constant. The PVCR, consequently, increased by a factor of two as the interrupt time was increased to 30 s. However, surprisingly the authors concluded that growth interrupts did not play a significant role in determining the electrical characteristics of DBRTDs [29].

In a related paper, Forster *et al.* have recently reported on the effect of interface roughness on the I - V characteristics of AlAs/InGaAs DBRTDs. These devices consisted of 17Å AlAs barriers with a 40Å pseudomorphic $In_xGa_{1-x}As$ quantum well and surrounding cladding layers which were embedded in heavily doped GaAs. The indium mole fraction was varied from 0 to 0.35 with the PVCR increasing up to 17% indium mole fraction and then decreasing rapidly. The authors attributed the increase in the PVCR of the DBRTDs to two reasons. First, due to the higher surface mobility of the indium atoms on the growth front, a reduction in the interface step density compared to an AlAs/GaAs interface grown

at the same temperature can be expected. Second, increasing the indium mole fraction will result in a higher conduction band offset between InGaAs and AlAs.

Unfortunately, the IBM study is not applicable to the optimization of DBRTDs for microwave oscillator applications. Such applications require the study of high current density and hence extremely thin barrier devices. Also, the interface roughening and smoothening is qualitatively different for very thin layers compared to layers several hundred angstroms thick. Further, they did not investigate the effects of interrupts at the normal AlGaAs/GaAs interface. The investigation by Foster et. al. also suffers several difficulties. Since it is difficult to separate the structural and band structure effects on the I - V characteristics, their interpretations of the experiment is questionable. Further, the pseudomorphic nature of the AlAs/InGaAs interface introduces strain effects that change the growth mode from two-dimensional layer growth to three-dimensional (pure island) growth mode [[30]]. This then introduces the additional uncertainty of dislocation induced current transport into the study.

2.5 Influence of growth interruption on the I-V characteristics of AlAs/GaAs DBRTDs

It is clear that further investigation of the effects of growth interruption and interface roughness on DBRTDs must be undertaken. In this section we will examine the influence of growth interruption on the I-V characteristics of thin barrier, high current density AlAs/GaAs DBRTDs. The interrupt durations used for the DBRTDs were based on the results of independent RHEED experiments. These consisted of measurements of the specular spot intensity oscillations during prototypical device growth sequences consisting of 6 ML AlAs, interrupt, 18 ML GaAs, interrupt, and finally 6 ML AlAs. Since it is well known that RHEED intensity oscillations are sensitive to diffraction conditions, care was taken to ensure that the RHEED diffraction conditions were identical for all experiments and there was no anomalous phase relationship [[31]]. The GaAs and AlAs growth

rates were 0.4 ML/s and 0.3 ML/s, respectively. The As/Ga beam equivalent pressure ratio was 30 (As BEP: 7.2 x 10^{-6} Torr) and the As/Ga flux incorporation ratio was 3.1 at a substrate temperature of 600°C.

The RHEED intensity oscillations during the prototypical device sequence growth as a function of interrupt duration are shown in Fig. 2.6.

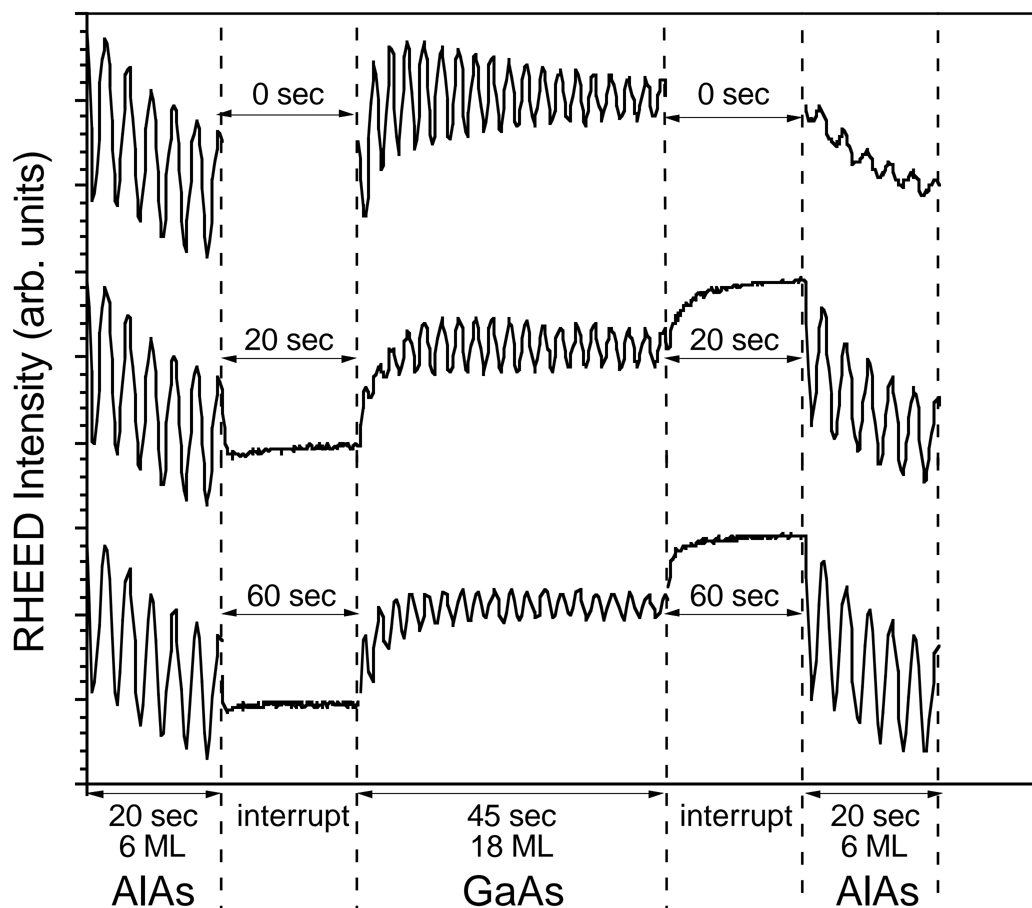

Fig. 2.6 Evolution of RHEED specular spot intensity oscillations during prototypical growth sequences consisting of 6 ML AlAs/interrupt/18 ML GaAs/interrupt/6 ML AlAs. The interrupt time was varied from 0 to 60 s. The interrupt time scales have been compressed to allow easy comparison of the relative oscillation amplitudes of the three layers.

This figure illustrates the evolution of the intensity oscillations as the interrupt time between layers is varied from 0 to 60 s. In this figure, the interrupt time scales have been compressed to allow easy visual comparison of the relative oscillation amplitudes of the three layers. In all cases, the RHEED oscillations were maintained throughout the entire growth sequence, which indicates that a two dimensional growth front was sustained. Also, very strong oscillations were observed during the growth of the first 6 ML AlAs layer. However, interruptions on AlAs did not result in specular spot intensity recovery, with the intensity remaining essentially constant until the GaAs quantum well growth was initiated. Furthermore, as the growth interruption was increased on AlAs, the GaAs grown on top of it became rougher as evidenced by a reduced oscillation amplitude during the GaAs quantum well growth. This may indicate that the very thin 6 ML AlAs layer was fairly smooth, and so growth interruption was not beneficial. In contrast to the behavior of the AlAs layer, specular spot intensity recovery was observed for interrupts on the 18 ML thick GaAs layer. If no interruption was used after the GaAs growth, the RHEED oscillations seen during the growth of the final AlAs layer were much worse than those seen during the growth of the first AlAs layer. However, a 60 s interruption on the GaAs layer was sufficient to produce oscillations from the final AlAs layer with amplitude comparable to that of the first AlAs layer.

For the case of 6 ML AlAs barriers, it is clear that a growth interruption after GaAs and not after AlAs is the desired interrupt schedule. In fact, such a schedule is shown in Fig. 2.7 where the RHEED oscillation during the deposition of 6 ML AlAs/18 ML GaAs/30 sec interrupt/6 ML AlAs is given. Here, a 30 sec interrupt after the GaAs layer is sufficient to recover the second AlAs layer oscillation amplitude to that of the first AlAs layer.

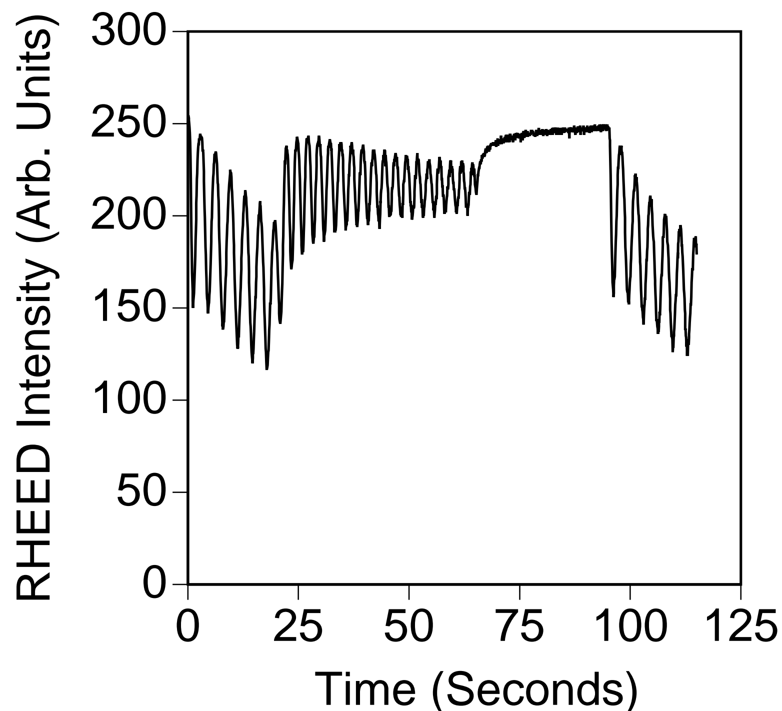

Fig. 2.7 RHEED intensity oscillations for a 6 ML AlAs/30 s interrupt/18 ML GaAs/AlAs layer sequence. A 30 s interrupt is sufficient to recover the second AlAs layer oscillation amplitude to that of the first AlAs layer.

However, it is interesting to examine if this conclusion holds for the case of AlAs layers thicker than 6 ML, for example, 15 ML thick. Shown in Fig. 2.8 is a plot of the RHEED intensity oscillations during the growth of 15 ML AlAs/Interrupt/18 ML GaAs.

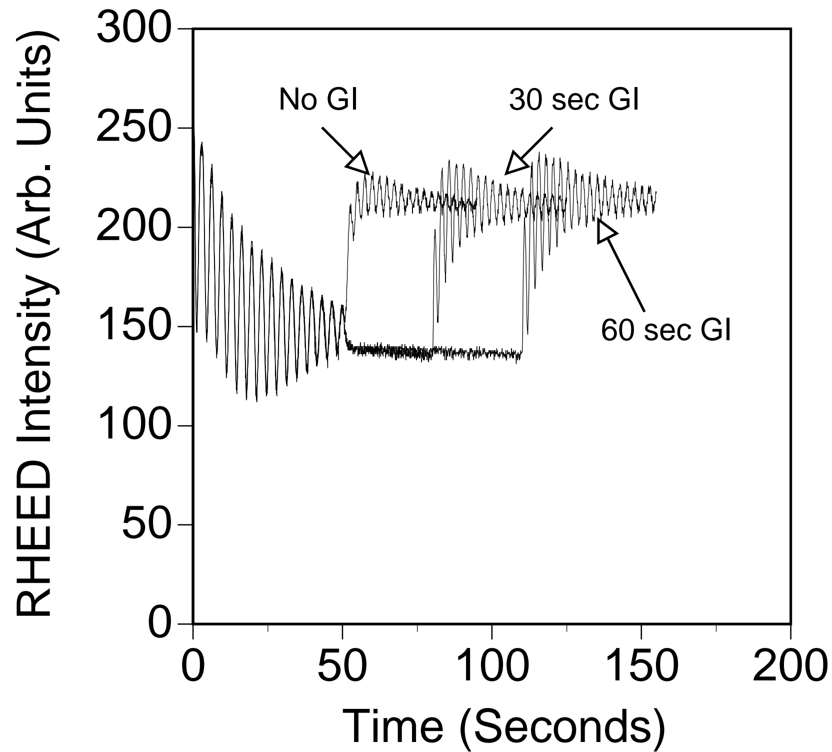

Fig. 2.8 RHEED intensity oscillations for a 15 ML AlAs/ interrupt/18 ML GaAs layer sequence. The interrupt time was varied from 0 to 60 s. The plots have been superimposed on each other. In contrast to the 6 ML AlAs case, an interrupt is shown to improve the GaAs grown on top of the AlAs.

Such a layer sequence would correspond to a DBRTD with 15 ML AlAs barriers and a 18 ML GaAs quantum well. Although such a device would not be useful as a microwave device due to the very low current densities, it is nevertheless instructive to study the RHEED oscillations during such a prototypical device layer sequence growth. The interrupt duration was varied from 0 s to 60 s and the plots have been superimposed on each other. There are several differences to note between the 6 ML AlAs and 15 ML AlAs examples. The 15 ML AlAs layer is roughening as indicated by the reduced oscillation amplitude, especially after seven ML of deposition. Further, as the interrupt time on the AlAs layer is increased, the GaAs grown on top becomes smoother as evidenced by the increased

oscillation amplitude. This is in contrast to the 6 ML AlAs case where an interrupt after AlAs resulted in a rougher GaAs grown on top of it. Consequently, it appears that the optimum interrupt schedule depends on the constituent layer thicknesses.

As the above discussion has shown, the interrupt schedule affects the interface quality. Therefore, it is possible it may also affect the device I-V characteristics. From the data shown in Fig. 2.6, it might be expected that a DBRTD grown using interruptions only after the growth of GaAs layers, and not after AlAs barrier layers, should improve the I-V characteristics over a device grown with no interruptions. Further, a device grown with long interruptions (60 s) after AlAs layers, but not after GaAs layers, might result in poorer characteristics compared to one grown with no interruptions.

To test this hypothesis, four structurally symmetric, baseline DBRTDs were grown at 600°C with different interruption schedules [[32]]. The growth conditions were nominally the same as those employed in the RHEED measurements. The layer schematic of the devices along with the interrupt schedule are given in Fig. 2.9.

Layer	Material
5000 A n+ (1.2 x 10^{18} cm^{-3})	GaAs
100 Ă n (4.3 x 10^{17} cm^{-3})	GaAs
100 Ă n - (6.0 x 10^{16} cm^{-3})	GaAs
50 A Undoped	GaAs
17 Ă Undoped	AlAs
50 Ă Undoped	GaAs
17 Ă Undoped	AlAs
50 Ă Undoped	GaAs
100 Ă n - (6.0 x 10^{16} cm^{-3})	GaAs
100 Ă n (4.3 x 10^{17} cm^{-3})	GaAs
5000 A n+ (1.2 x 10^{18} cm^{-3})	GaAs
n+ GaAs Substrate	

Growth Interrupt Schedule

Sample A	Sample B	Sample C	Sample D
0 s	20 s	60 s	0 s
0 s	0 s	0 s	60 s
0 s	20 s	60 s	0 s
0 s	0 s	0 s	60 s
0 s	20 s	60 s	0 s
0 s	20 s	60 s	0 s

Fig. 2.9 Layer schematic of the DBRTD structure along with the interrupt schedule for the four DBRTDs studied.

Sample A, the control, is grown without any interruption. For samples B and C, growth interruptions of 20 and 60 s, respectively, were employed after the GaAs layers, while no interruptions followed the growth of the AlAs layers. For sample D, growth interruptions of 60 s only on the AlAs layers were used, with no interruptions on the GaAs layers. All samples, grown on (100) n+ GaAs substrates, consisted of a nominally undoped (n type, 1 x 10^{15} cm^{-3}) 18 ML GaAs quantum well sandwiched between 6 ML AlAs barriers, followed by a three-step dopant transition region consisting of 50Å of nominally undoped GaAs adjacent to the AlAs barriers, 100Å of n type, 6 x 10^{16} cm^{-3} GaAs and finally 100Å of n-type, 4.3 x 10^{17} cm^{-3} GaAs.

Mesa-isolated devices were fabricated through a photolithographic, lift-off process that is outlined in the Appendix. The electrical measurements are performed with a computerized data acquisition system. The I - V measurements were performed with a Keithley K230 programmable voltage source and a K195A digital multimeter. Ten to fifteen devices per sample were tested. The measured I - V data for samples A, B, C, and D are summarized in Fig. 2.10.

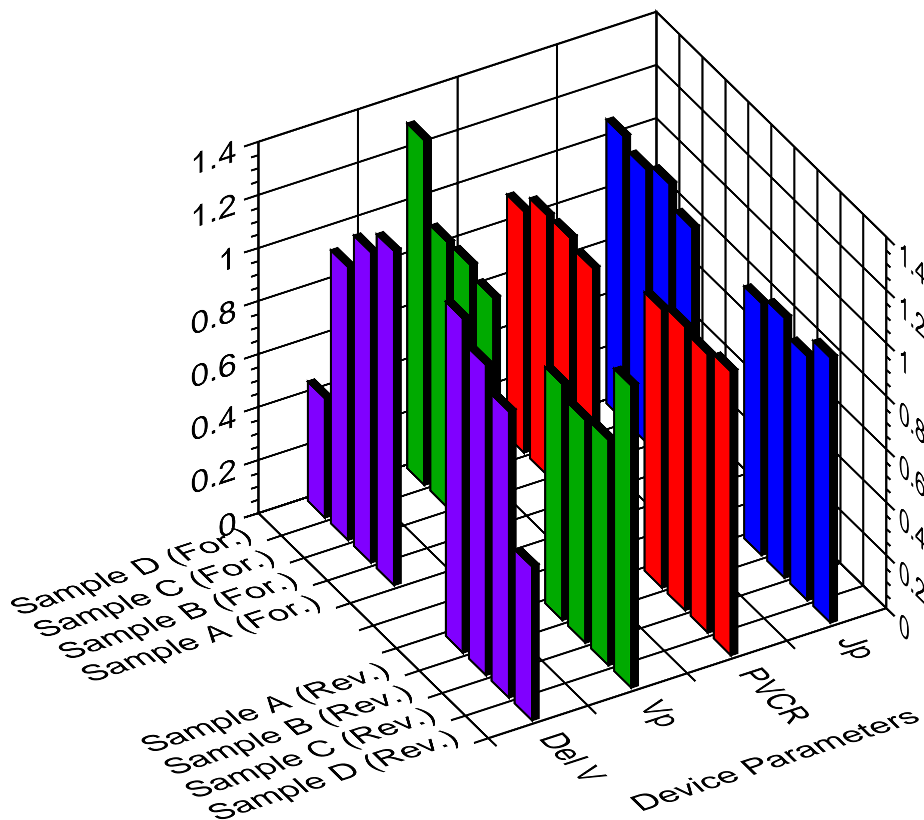

Fig. 2.10 Summary of measured I - V data for samples A, B, C, and D. The values for J_p, PVCR, V_p, and ΔV are normalized to their respective averages based on all samples and both bias directions. The average values for J_p, PVCR, V_p, and ΔV were 43 kA/cm^2, 4.4, 0.83 V, and 0.22 V. The standard deviations for all quantities presented were less than 5%.

This figure shows normalized values for peak current density (J_p), peak-to-valley current ratio (PVCR), peak voltage (V_p), and difference between peak and valley voltages (ΔV) for both electron injection through the bottom barrier first (forward bias) and for injection through the top barrier first (reverse bias). The quantities are scaled to their respective averages based on all samples and both bias directions. The average values for J_p, PVCR, V_p, and ΔV are 43 kA/cm^2, 4.4, 0.83 V, and 0.22 V, respectively. The same data with one standard deviation is also given in tabular form in Table 2.1. In addition, I - V data for a DBRTD , Sample D*, that was grown during a previous system cycle but with an interrupt schedule similar to that of sample D is also given in Table 2.1.

Device Parameters	Sample A	Sample B	Sample C	Sample D	Sample D*
PVCR (For.)	4.0 +/- 0.2	4.1 +/- 0.2	4.1 +/- 0.2	3.8 +/- 0.2	3.8 +/- 0.1
PVCR (Rev.)	4.4 +/- 0.1	4.5 +/- 0.2	4.4 +/- 0.1	4.2 +/- 0.2	4.5 +/- 0.1
J_p (For.)	44 +/- 1.7	47.5 +/- 2.2	46 +/- 2	48 +/- 2.2	40 +/- 1
J_p (Rev.)	42.5 +/- 1.8	44 +/- 1.9	41 +/- 2	45 +/- 2	37 +/- 1
V_p (For.)	0.80 +/- 0.02	0.83 +/- 0.02	0.84 +/- 0.03	1.10 +/- 0.02	0.78 +/- 0.03
V_p (Rev.)	0.74 +/- 0.02	0.70 +/- 0.02	0.71 +/- 0.03	0.95 +/- 0.02	0.67 +/- 0.03
ΔV (For.)	0.28 +/- 0.02	0.26 +/- 0.02	0.23 +/- 0.03	0.1 +/- 0.02	0.26 +/- 0.02
ΔV (Rev.)	0.28 +/- 0.02	0.26 +/- 0.02	0.24 +/- 0.03	0.13 +/- 0.02	0.27 +/- 0.02

Table.2.1 Tabular representation of data presented in Fig. 2.10. The parameter values reported here are state-of-the-art for devices with these dimensions.

Comparing the data for samples A, B, C, and D, J_p and PVCR are independent of both the interrupt time and schedule. The V_p and ΔV appear to be sample dependent in that a higher V_p and smaller ΔV is obtained in sample D (60 s growth interruption on AlAs only). Although this may be due to the interrupt schedule, it could also be due to parasitic series resistance. In fact, as shown in Table 2.1, sample D* exhibits characteristics similar to samples A, B, and C. Moreover, the PVCR in reverse bias is among the highest of all the samples. Therefore, it is not clear whether the growth interruption on AlAs has a significant impact on the I - V characteristics. Surprisingly the 60 s growth interruption on GaAs did not improve the PVCR and J_p even though the RHEED measurements indicated that this interrupt schedule did cause significant interface smoothing. From the data presented here, it is concluded that interface roughness present in our thin barrier, high current density AlAs/GaAs DBRTDs does not play significant role in determining electrical characteristics.

All the DBRTDs studied here, regardless of interrupt schedule, display a slight asymmetry in both PVCR and J_p between forward and reverse bias. Electron injection from top to bottom (reverse bias) results in higher PVCR and lower J_p, whereas for electron injection from bottom to top (forward bias), the PVCR is lower and the J_p is higher.

How do our experimental observations compare with theoretical predictions of the effect of interface roughness on the I- V characteristics? By and large, these treatments are either relatively simplistic or do not calculate I-V characteristics. An example of the first type of calculation is that by Bruno *et al.* [33]. The I-V characteristic of the real diode (with interface roughness) is given by a weighted average of the I-V characteristics of ideal (flat interfaces) DBRTDs of differing dimensions that are connected in parallel. The weights are determined by the probability, calculated through a binomial distribution, of occurrence in the real diode. They then use a Tsu-Esaki coherent transport model, which will be discussed in the next chapter, to calculate the I - V characteristics. Two

assumptions are made in the transport model to reduce the three dimensional problem of interface roughness to a one dimensional problem. First, the electrons have a coherence length much greater than the active region width. Second, the coherence length is much smaller than λ, where λ is the average planar dimension of regions composed of only one type of material. The device simulated was a low barrier height (318 meV) AlGaAs barrier DBRTD. They calculated I-V characteristics for an ideal diode and a "real" diode. The real diode had a geometry that corresponded to less than 0.2% of the diode's lateral area being of nominal thickness. They observed no significant difference in the I-V characteristics between the two diodes. Hence, they concluded that interface roughness does not play a significant role in these devices. However the assumption in Bruno's model that the coherence length be much smaller than λ may not be realistic. In fact, if the coherence length is on the order of λ, then the interface roughness can result in state mixing through elastic scattering. Such a possibility is not treated in this model.

A more sophisticated model to treat interface roughness has been recently put forward by Ting and McGill [[34]]. They employed a tight-binding model where each monolayer was divided into planar supercells. Within each supercell, the lateral potential could be specified. They calculated transmission coefficients versus incident electron energy, T(E) vs. E, for a set of AlAs/GaAs double barrier structures with a GaAs quantum well width of twelve monolayers and a barrier thickness of four monolayers. Then, for the AlAs/GaAs interface on the incident electron side, a random coverage interfacial layer was placed between the pure GaAs and AlAs layers. The configuration of this interfacial layer was determined by a simulated annealing algorithm. Island sizes from 28Å to 106Å were used in the T(E) vs E calculations. The peaks in the transmission coefficient for all structures were similar. However, as the island size increased, satellite peaks appeared and increased in magnitude. The satellite peaks are a result of electrons being scattered parallel to the hetero-interface. If the island size is increased even

further, the transmission coefficient peak broadens and the satellite peaks disappear as a result of wave function localization.

The real question, however, is how Ting *et al.* results translate into I-V characteristics. Unfortunately, they did not present calculated I - V characteristics. If we are to assume that the tunneling current is a convolution of the incident electron supply function and the transmission coefficient, increasing the island size should result in a lower PVCR due to the increased satellite peak height and broadening of the transmission peak. However, to relate their calculations to our measured data requires knowledge of the interfacial structure of our DBRTDs. This is possible only through very high resolution chemical lattice images of the DBRTD interfaces. This is an extremely expensive and time-consuming venture and was not possible during the course of this work.

An intriguing observation apparent in the data presented in Table 2.1 is that, regardless of interrupt schedule, there is asymmetry in the PVCR and J_p between forward and reverse bias. Electron injection from top to bottom (i.e., reverse bias) results in higher PVCR and lower J_p, whereas for electron injection from bottom to top (forward bias), the PVCR is lower and the J_p is higher. At first glance this is not a surprising result, given that the interface roughness at the four heterointerfaces of the DBRTD is different due to the different surface adatom mobility of the gallium and aluminum cations. Leo and MacDonald have theoretically examined this asymmetry issue [[35]]. They studied the effect of elastic scattering on electron tunneling through DBRTD structure by representing the interface roughness as a perturbation potential in a Green's function formalism. The structure consisted of two 30Å AlGaAs barriers, 270 meV high separated by a 30Å GaAs quantum well. They concluded that the effect of roughness on the transmission coefficient depends on the location of the rough interface. Specifically, since the inverted interface (GaAs grown on AlGaAs) is rougher than the normal interface (AlGaAs grown on GaAs), electrons incident towards the substrate encounter the rougher, inverted interface first. Similar to Ting *et al.*,

these observations are based on transmission coefficient calculations. However, the authors believe that the asymmetries seen in the T(E) vs E curves should be observable in the I-V characteristics. Therefore, Leo *et al.*'s results predict a higher PVCR for electron injection from the substrate to the top than for electron injection towards the substrate. These predictions are opposite to what is seen in our data; a higher PVCR is obtained for reverse bias, where electrons encounter a nominally rougher AlAs interface first. We believe the observed asymmetry is due to a growth-induced thickness asymmetry, which yields a top AlAs barrier that is slightly thicker than the bottom AlAs barrier [36]. These observations suggest that further work is needed in developing both theoretical models and in obtaining experimental data on interface quality in DBRTDs.

2.6 MBE Growth of InAlGaAs on InP

The discussion so far has focused on the optimization of growth conditions for high performance DBRTDs fabricated in the AlAs/GaAs material system. The use of RHEED to rapidly and reproducibly determine optimum growth conditions was highlighted. Also, growth interrupts at heterointerfaces were shown not to have a significant or even a beneficial effect on the electrical characteristics of high current density AlAs/GaAs DBRTDs.

However, to improve DBRTD performance further for microwave oscillator applications, devices should be fabricated in the InAlGaAs/InP material system. Specifically, this requires the growth of InGaAs, lattice matched to InP, as the quantum well and cladding material, and pseudomorphic AlAs serving as the barrier layers. The choice of this material system is based on the superior transport characteristics due to its bandstructure. These characteristics will be discussed in Chapter 3. In this section, we will focus on the MBE growth of high quality, lattice-matched InGaAs and strained or pseudomorphic AlAs.

2.6.1 Growth issues for lattice-matched InGaAs on InP

The growth of $In_xGa_{1-x}As$ on InP is more complicated than the growth of AlGaAs on GaAs due to the stringent lattice matching requirement. This can be seen in Table 2.2, which shows the lattice constants and mismatch of the constituent binary alloys in the InAlGaAs/InP material system. The ternary alloy is lattice matched to InP at only one alloy mole fraction, x = 0.532. An indium rich epilayer ($x > 0.532$) and an indium deficient epilayer ($x < 0.532$) will have a lattice constant larger and smaller, respectively, than that of InP.

Material	Lattice Constant (Å)	Mismatch (%): $(a_{epi} - a_{sub})/a_{sub}$
GaAs	5.6532	- 3.7 % on InP
InP	5.8687	+ 3.8 % on GaAs
InAs	6.0583	+ 3.2 % on InP
AlAs	5.6611	- 3.5 % on InP
$In_{0.532}Ga_{0.468}As$	5.8687	-

Table 2.2. Lattice constant and mismatch in the InAlGaAs/InP material system.

This lattice matching constraint, therefore, requires tight control over the mole fraction throughout the entire growth sequence. Large deviations from the lattice matching condition can result in heavily dislocated material with poor electrical characteristics [37], degraded optical quality [38], and rough surface morphology [39]. In practice, however, a small amount of lattice mismatch is always present and it is a question of how much is tolerable for the application at hand.

As discussed earlier in the chapter, the growth parameters that need to be optimized are the substrate temperature, growth rates, and the arsenic overpressure. The optimum substrate temperature for $In_{0.53}Ga_{0.47}As$ growth is between the optimum temperature for InAs (~ 450°C) and GaAs (~ 600° C) growth. Further,

the indium sticking coefficient above 540°C is significantly less than one and this places an upper temperature limit. The temperature window is therefore quite narrow. We have adopted a growth temperature of 505°C, the InP oxide desorption temperature, [40] for two reasons. First, as the oxide desorption and hence the growth temperature is accurately known, variations in growth temperature from run to run are no longer a concern. Second, material grown in the temperature range of 490°C to 510°C has shown excellent electrical and optical properties [41].

The choice of growth rates is again influenced by the lattice matching requirement. A higher InGaAs growth rate is desirable because variations in the binary InAs and GaAs growth rates will have a smaller impact. For example, if the GaAs growth rate drifts by 0.02 ML/sec, the indium mole fraction will drift by 2.2% and 3.7% for a InGaAs growth rate of 1.0 ML/sec and 0.6 ML/sec, respectively. Further, to keep the indium mole fraction variation below 1 %, the indium and gallium cell temperatures must be controlled to within 0.3°C. During the course of this work, we occasionally encountered problems with the indium cell temperature stability. The cell temperature and hence the flux would oscillate or 'motorboat' about the set point. Attempts to solve this problem were unsuccessful and it was later speculated that some form of unintended thermal feedback was affecting the cell temperature controller. Fortunately, this problem was not encountered very often and our overall experience with lattice matching has been quite favorable.

In addition to the lattice matching requirement, a much higher arsenic overpressure is required for InGaAs growth than for GaAs growth. This is due to the binding energy of the indium adatoms being lower than that of the gallium adatoms [42]. Therefore, a higher arsenic overpressure is necessary to prevent surface indium segregation. Too low an arsenic overpressure will result in indium clustering into metallic droplets and irreversible surface degradation. The arsenic BEP typically used for an incorporation ratio of 1.6 at a growth rate of 1 ML/sec

and a substrate temperature of 505°C is about 1.1 to 1.3 x 10^{-5} Torr. This value is a factor of two greater than that for GaAs growth.

2.6.2 InGaAs Growth Rate Calibration

The required InAs and GaAs growth rates for lattice matched InGaAs can be obtained through two methods: the BEP flux and RHEED oscillation techniques. Early in the course of this work, the BEP flux method was used for growth rate calibration. This procedure involves measuring the BEP of the indium and gallium sources. The indium and gallium cell setpoints are adjusted to obtain an indium to gallium flux ratio of between 2.0 and 2.2 [43]. However, BEP measurements of metal sources compared to arsenic are more involved since the ion gauge response is affected by metal atoms that are deposited on the filament. Also, the BEP of a metal source at typical growth rates is at least an order of magnitude smaller than the arsenic BEP, therefore the background arsenic pressure should be as low as possible before measuring the metal BEP. This typically requires waiting at least thirty minutes for the background arsenic to be pumped away. The metal BEP is then taken as the difference between the BEP reading with the metal cell shutter open and the reading with the shutter closed. The ion gauge sensitivity is then recovered by opening the arsenic shutter and exposing the filament to arsenic for five to ten minutes. This is believed to result in the formation of InAs or GaAs at the filament which is then desorbed and pumped away. To obtain reliable values, the BEP measurement cycle including the arsenic clean should be repeated several times. This is an extremely time consuming procedure and was abandoned in favor of the RHEED oscillation method described next.

Growth rate calibrations with RHEED are attractive for two reasons. First, it is more reliable and quicker than the BEP method. Second, due to time and system constraints, one does not have the luxury of growing several layers with different growth parameters and carefully characterizing each layer to providing

feedback. Through RHEED, one can calibrate the growth rates required for lattice matched growth quickly and grow high performance devices.

It was shown in Sec. 2.3 (Eq. 2.2) that RHEED can be used to determine the alloy composition. In order to grow lattice matched InGaAs, the growth rates of the binary constituent alloys, InAs and GaAs, must be adjusted accordingly. For an $In_{0.532}Ga_{0.468}As$ growth rate of 1 ML/sec, the GaAs and InAs growth rates *on InP* must be 0.468 ML/sec and 0.532 ML/sec, respectively. Due to the unequal lattice constants, the equivalent growth rates, R, of the binary alloys are:

$$R(\text{GaAs on GaAs}) = (0.468 \text{ ML/sec}) * \left(\frac{a_{GaAs}}{a_{InP}}\right)^2 = 0.434 \text{ ML/sec} \quad (2.4a)$$

$$R(\text{InAs on InAs}) = (0.532 \text{ ML/sec}) * \left(\frac{a_{InAs}}{a_{InP}}\right)^2 = 0.567 \text{ ML/sec} \quad (2.4b)$$

The square of the ratio of the lattice constants in Eq. 2.4 compensates for the growth rates being different on substrates having different lattice constants. For a given incident flux, the monolayer deposition rate on GaAs will be smaller than on InP, since more atoms are required for monolayer formation on GaAs than for InP. The GaAs growth rate can, of course, be easily obtained. However, measurement of the InAs growth rate is more involved. Due to the lack of high quality InAs substrates [[44]], one must grow strained, lattice mismatched $In_xGa_{1-x}As$ on GaAs. In practice, strained $In_xGa_{1-x}As$ grown on GaAs results in strongly damped RHEED oscillations, so the indium mole fraction must be limited to less than 0.25 for reliable measurements [[45]] A further complication is that the substrate temperature must be kept below 550°C to prevent indium adatom reevaporation, thereby also resulting in poor strained InGaAs oscillations due to low adatom mobility. The key is to get the indium growth rate, as measured on the GaAs substrate, close as possible to the lattice matching condition, Eq. 2.4. Then, one can deposit the InGaAs layers on InP and fine tune the indium cell setpoint by monitoring the growth rates with the RHEED oscillations.

To illustrate this procedure, assume we want an $In_{0.532}Ga_{0.468}As$ growth rate of 1.0 ML/sec. This means that the InAs growth rate on GaAs should be $(5.8687/5.6532)^2 * 0.532$ ML/sec = 0.494 ML/sec. First, a GaAs growth rate of 1.2 ML/sec at a substrate temperature of 520°C must be obtained. Then, increase the indium cell setpoint until the $In_xGa_{1-x}As$ growth rate is 1.6 ML/sec. The increase in the indium cell setpoint should be taken in small steps. The arsenic flux should also be increased to compensate for the higher growth rate. At this growth rate, the indium mole fraction would be 0.25 and RHEED oscillations should still be observable. The equivalent InAs growth rate would be $(5.8687/5.6532)^2 * 0.4 = 0.44$ ML/sec. This value is close enough to begin calibrations on the InP substrate. The gallium cell setpoint is kept the same since it is already set at the proper growth rate. The indium setpoint is then increased in small steps and

InGaAs RHEED oscillations monitored until the InGaAs growth rate on InP is 1.0 ML/sec. Initially, the deposited InGaAs layers will be strained so their thickness should be no more 50Å. As the indium setpoint gets closer to the lattice match value, the RHEED oscillations will improve and thicker layers can be grown. Shown in Fig. 2.11 is a RHEED intensity plot for a lattice matched InGaAs layer on InP.

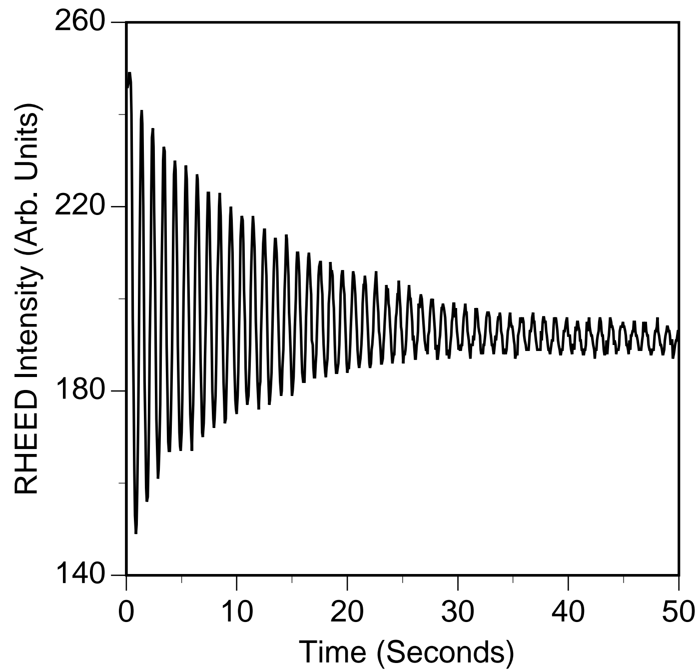

Fig. 2.11 RHEED intensity oscillations for lattice matched InGaAs layer on a InP substrate.

The growth rate is 1.0 ML/sec and fifty oscillations have been recorded. The large number of oscillations demonstrate that smooth growth fronts can be achieved and a high degree of interface perfection can be expected in InGaAs heterostructures.

2.6.3 Critical Layer Thickness and Strained Layer Growth

We have just discussed the procedure for growing lattice matched InGaAs, the material that will serve as the quantum well and cladding layers. The growth of the AlAs barrier layers raises the issue of strained layer or pseudomorphic growth. When an epilayer is deposited on a substrate with a different lattice constant, the epilayer's crystal structure must initially undergo elastic distortion to maintain registry with the substrate. For thin epitaxial layers and a moderate amount of

lattice mismatch (< 7%), the mismatch can be accommodated by elastic strain until a critical layer thickness, h_c, is reached [46]. Once the critical thickness has been reached, it is energetically favorable for the creation of a misfit dislocation to reduce the strain energy. In this work, devices with AlAs layers below and above the critical layer thickness have been fabricated.

Fig. 2.12 illustrates the epilayer arrangement for AlAs growth on $In_{0.532}Ga_{0.468}As$ or InP during both strained layer growth and relaxed layer growth.

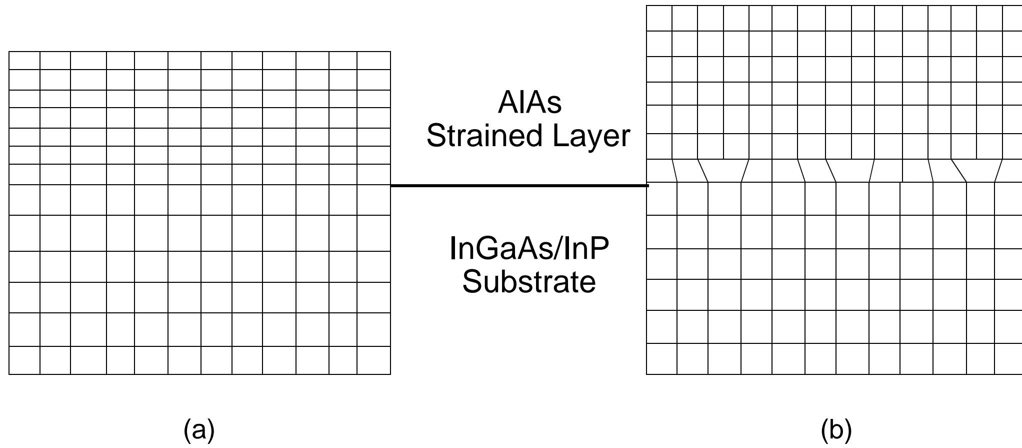

Fig. 2.12 Schematic of (a) strained and (b) relaxed AlAs on lattice matched InGaAs or InP. The strained AlAs layer maintains its registry with the substrate by biaxial in-plane tension and tetragonal compression in the perpendicular, growth direction. The AlAs layer relaxes through the creation of misfit dislocations at the epilayer/substrate interface.

During strained layer growth, as shown in Fig. 2.12a, the epilayer will undergo biaxial in-plane tensile extension along with a tetragonal compression in the perpendicular, growth direction since the AlAs lattice constant of 5.6611Å is less than the $In_{0.532}Ga_{0.468}As$ lattice constant of 5.8687Å. The AlAs epilayer in-plane and out-of-plane lattice constants, as calculated from elasticity theory, are given by:

$$a_{in-plane} = a_{InP} \tag{2.5a}$$

$$\varepsilon_{xx} = \frac{a_{InP} - a_{AlAs}}{a_{AlAs}} \tag{2.5b}$$

$$a_{out-of-plane} = \left(1 - 2\frac{C_{12}}{C_{11}}\varepsilon_{xx}\right)a_{AlAs} \tag{2.5c}$$

where the ratio of elastic stiffness constants, C_{12}/C_{11}, is equal to 0.47 [47].

These equations assume that the substrate thickness is much greater than the epilayer thickness, and therefore the strain is confined to the epilayer only. Further, Eq. 2.5c illustrates the tetragonal distortion that must occur when the in-plane lattice constant is forced to equal the substrate lattice constant. Then, the AlAs out-of-plane lattice constant for growth on $In_{0.532}Ga_{0.468}As$ is 5.46Å or 2.73Å/ML.

When h_c is surpassed the epilayer relaxes to its natural lattice constant through the creation of edge misfit dislocations as shown in Fig. 2.12(b). There are two models for the calculation of the critical layer thickness. The Van der Merwe theory or energy balance model assumes the critical layer thickness is reached when the strain energy density caused by the lattice mismatch equals the minimum energy density for misfit dislocation generation [48]. In the Matthews-Blakeslee theory or force balance model, the critical layer thickness is reached when the force exerted on a dislocation line by the stress is equal to the tension in the dislocation line [49].

Critical layer thicknesses in the InGaAs/GaAs and InGaAs/InP material system have been determined by Hall-effect measurements [50], transmission electron microscopy, quantum well photoluminescence [51], and p-i-n diode reverse leakage currents [52]. The critical layer thickness inferred from these experiments is well described by the Matthews-Blakeslee force balance model and tends to be overestimated by the Van der Merwe energy balance model. Therefore, we take the critical layer thickness to be given by the force balance expression as [53]:

$$h_c = \frac{a}{\sqrt{2}} \frac{\left(1 - \sigma/4\right)}{2\pi\varepsilon(1+\sigma)} \left[\ln\left(h_c \frac{\sqrt{2}}{a} \right) + 1 \right] \tag{2.6}$$

where a is the substrate lattice constant, σ is Poisson ratio, and ε is the lattice mismatch, ε_{xx} (Eq. 2.5b). For AlAs/$In_{0.532}Ga_{0.468}As$, with a = 5.8687Å, σ = 0.32, and ε = 0.036, h_c is calculated to be approximately 40Å. Eq. 2.6 is a first order approximation that should be used only as a rough estimate since the temperature dependent kinetics of the misfit dislocation generation process are not considered. Further, metastable layers can be grown at low temperatures that are coherently strained well past their expected critical layer thickness [54]. Nevertheless, the force-balance model provides a conservative estimate that is useful during device design. In practice, h_c must be empirically determined through a measurement technique that reflects the device application at hand. For example, inferring critical layer thicknesses from Hall effect mobility measurements may not be directly relevant for optoelectronic devices.

The structural nature of the pseudomorphic AlAs/InGaAs interface has been recently investigated by in-situ laser light scattering (LLS) and high resolution TEM. Briefly, in the LLS technique, the reflection of diffuse or off-specular laser radiation from the wafer surface is monitored during layer deposition [55]. When dislocations are formed, the surface roughness and hence the reflected light intensity increases. The critical layer thickness is then taken as the deposited layer thickness when an abrupt increase in the scattered light intensity is detected. The h_c determined from the LLS technique is approximately 30Å for AlAs grown on $In_{0.532}Ga_{0.468}As$ at 500°C and has been corroborated by acoustic force microscopy measurements [56]. Also, high resolution TEM or chemical lattice imaging measurements have been made on AlAs layers with varying layer thicknesses embedded in lattice matched InGaAs [57]. It was observed that AlAs layers 20Å and 30Å thick were defect free while those 50Å and thicker exhibited dislocations. These results are in surprisingly close agreement with the calculated value of

approximately 40Å and suggest that this value be used as a benchmark during device design.

2.7 InAlGaAs Epilayer Characterization

The AlAs and InGaAs epilayers were characterized by Nomarski optical microscopy, X-ray diffraction, photoluminescence, and Hall-effect mobility measurements. Except for the mobility measurements, these techniques are non-destructive. Nomarski optical microscopy is the simplest and, by examining the surface morphology, can provide insight into the growth kinetics and dislocation formation. The lattice mismatch of the InGaAs epilayers can be rapidly determined by X-ray crystal diffraction and provide feedback for the adjustment of the growth rates on subsequent layers. The photoluminescence and Hall-effect mobility measurements characterized the impurity concentrations, which influence minority carrier based devices such as lasers, detectors, and bipolar transistors.

2.7.1 Nomarski Optical Microscopy

Nomarski optical microscopy is very useful for delineating surface features on epitaxial layers since features of different elevations appear as different colors [58]. This contrast is achieved by splitting the illuminating beam into two beams displaced by a small distance, reflecting off the surface, and finally recombining the reflected beams. A presence of a step will change the optical path length and produce a contrast change in the reconstituted beam.

Shown in Fig. 2.13 is a Nomarski micrograph of a nominally lattice matched, 0.64 μm thick InGaAs epilayer. The film is generally featureless except for oval defects and surface preparation introduced defects. The slight surface color gradation apparent in the micrograph is due to the scanning and digitizing process, and is not present on the sample.

Fig. 2.13 Nomarski micrograph of MBE#2511 (0.64 μm InGaAs layer nominally lattice matched to InP).

Lattice matched films typically have a mirror-like finish. However, they occasionally exhibit a slight "orange peel" surface as shown in Fig. 2.14. Although it may not be clear in the micrograph reproduction shown below, the surface is grainy with some surface roughness and resembles that of an orange peel.

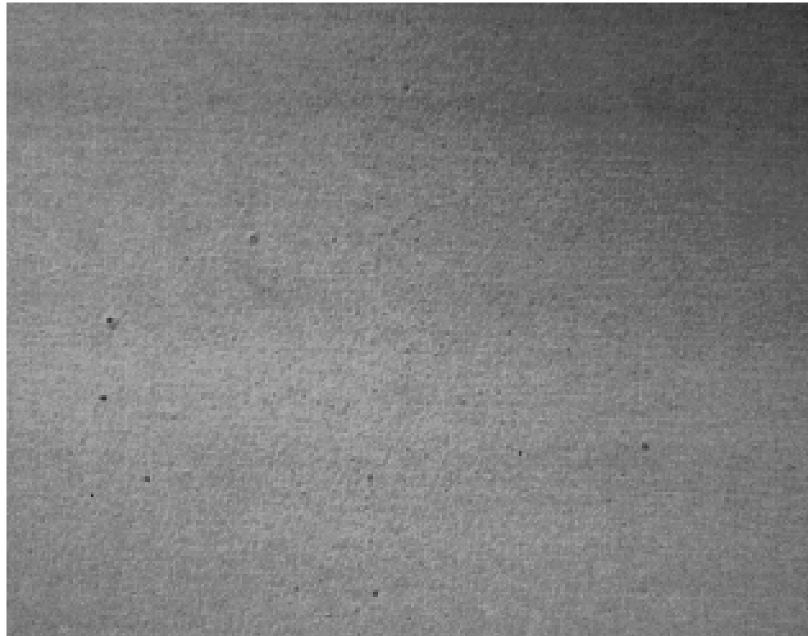

Fig. 2.14 Nomarski micrograph of MBE#2445 (1 µm InGaAs on InP) exhibiting an "orange peel" surface.

This usually indicates that the sample is slightly arsenic deficient and that the arsenic overpressure may have decreased during growth. This can cause indium surface segregation and result in the rough or "orange peel" surface. The electrical characteristics of DBRTDs with the "orange peel" surface are, however, similar to those with a mirror-like surface. Optical devices may, on the other hand, be affected by such a surface since it may increase optical scattering losses and waveguiding efficiency.

As discussed in the previous section, misfit dislocations will be generated if a strained layer's thickness is greater than the critical layer thickness. The heterojunction barrier varactor diodes that will be discussed in Chapter 4 employ strained AlAs barriers with thicknesses greater than the AlAs h_c on lattice matched InGaAs (~ 40Å). A Nomarski micrograph of a 50Å thick AlAs layer embedded in lattice matched InGaAs is given in Fig. 2.15. Parallel undulations along one

direction are clearly visible and correspond to misfit dislocations created at the AlAs/InGaAs interfaces. This behavior is particular to mismatched AlAs epilayers grown on lattice matched InGaAs [[59]]. This type of topography is not equivalent to the "cross-hatching" commonly seen in severely lattice mismatched InGaAs layers [[60]].

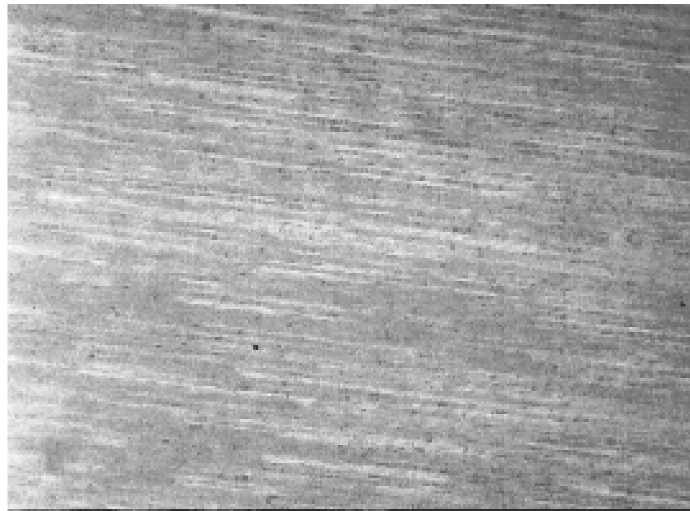

Fig. 2.15 Nomarski micrograph of MBE#1417 showing surface undulations in one direction only. This sample contains a 50Å AlAs epilayer embedded in lattice matched InGaAs.

An extreme consequence of lattice mismatched growth is given in Fig. 2.16. This figure shows the surface topography of a 1 μm InAs epilayer on GaAs. The lattice mismatch between InAs and GaAs is 7% and h_c is approximately 10Å. Hillocks consisting of concentric steps are clearly visible and are due to the enhanced growth at surface defects [[61]].

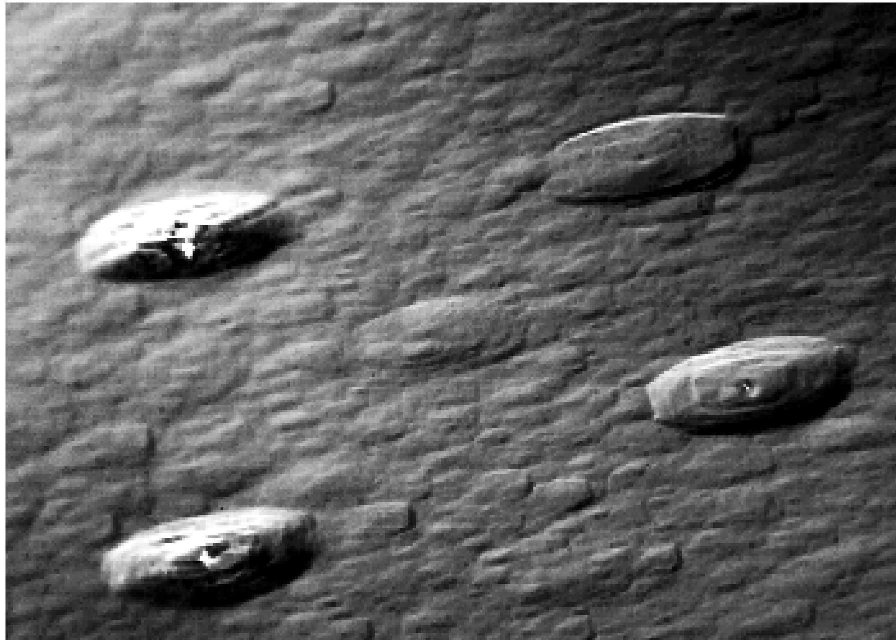

Fig. 2.19 Nomarski micrograph of MBE#1674 (1 μm InAs on GaAs) showing hillock formation due to misfit dislocations.

2.7.2 X-Ray Crystal Diffraction

X-ray diffraction provides a quantitative determination of the magnitude and sign of mismatch of epilayer lattice mismatch by measuring the spacing between planes parallel to (100) direction [62]. During the early part of this work, a single crystal X-ray diffraction (SCXRD) system (owned by Prof. Steinfink, Dept. of Chemical Engineering, Univ. of Texas at Austin) was employed to measure the lattice mismatch. A schematic of this system is shown in Fig. 2.17 (upper half of figure). This system was designed to measure diffraction patterns from powder samples, so it uses a source filter that sacrifices narrow spectral width for high intensity. The angle θ is the incident angle for X-rays impinging on the sample surface. The angle 2θ is defined as the angle between a line that specularly reflects off the sample to the detector and a line that passes straight through the sample

from the source. As the sample is rotated the diffractometer plots the detected intensity as a function of the angle 2θ.

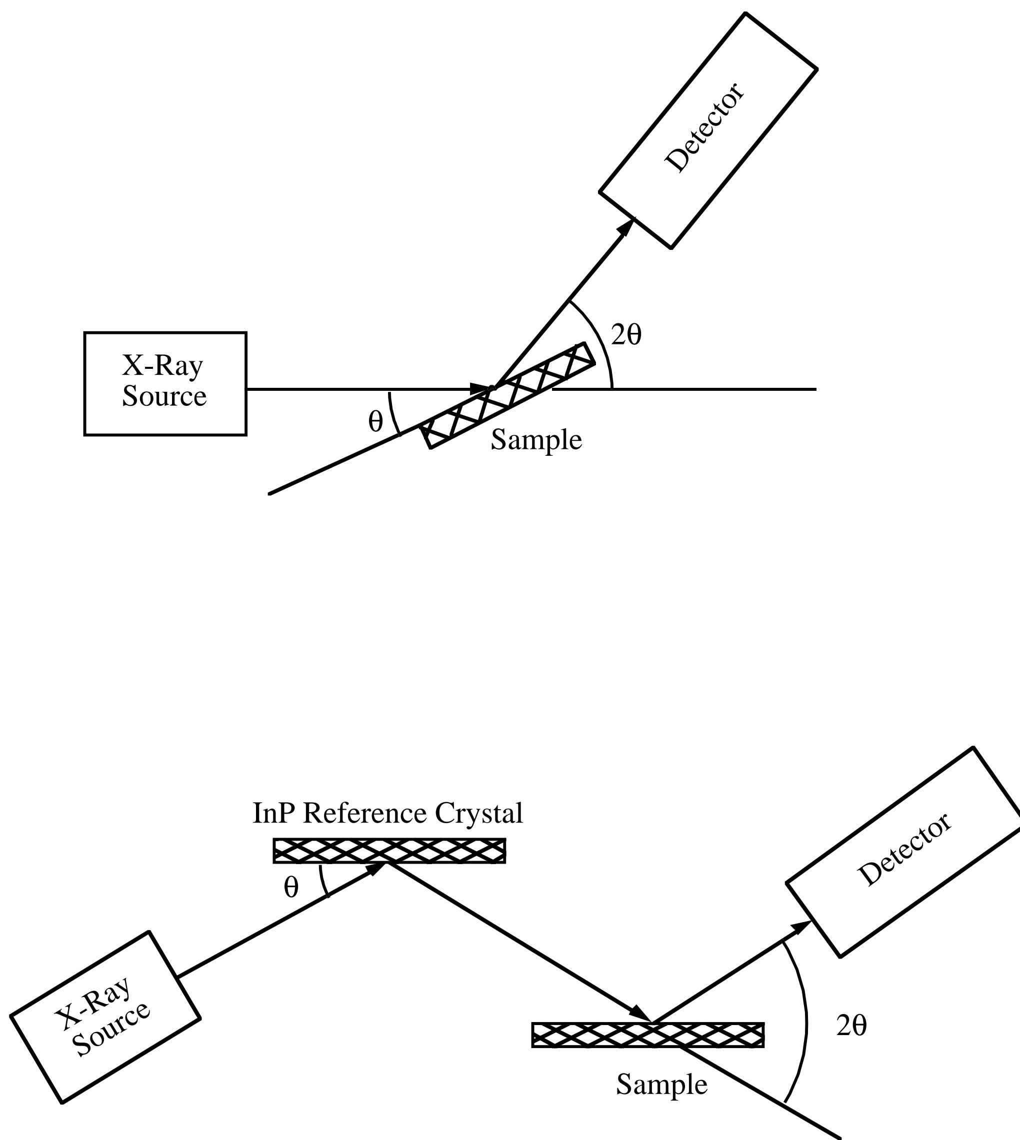

Fig. 2.17 Schematic of single crystal X-ray diffraction (SCXRD) system and double crystal X-ray diffraction (DCXRD).

Extraction of the epilayer lattice constant can be easily understood by considering Bragg's law:

$$2d_{hkl}\sin\theta = \lambda \quad \text{or} \tag{2.7a}$$

$$2\theta = 2\arcsin\left(\frac{\lambda}{2d_{hkl}}\right) \tag{2.7b}$$

where λ is the incident wavelength, θ is given in Fig. 2.17, and d_{hkl} is the spacing between parallel atomic planes. For a given λ and all d_{hkl}'s present in the crystal, Bragg's law will be satisfied only by a certain number of angles θ. Therefore, a plot of the diffracted intensity versus θ or 2θ should show a set of peaks corresponding to the atomic planes in the crystal. The location, intensity and width of these peaks provides the epilayer's lattice constant and crystalline quality, respectively.

The X-ray source generates two wavelengths, the Cu Kα1 (λ = 1.5405Å) line and the weaker Cu Kα2 (λ = 1.5443Å) line. With an InP crystal in the diffractometer, there is a signal peak at 2θ = 63.335° corresponding to the Cu Kα1 line and the (400) spacing of InP (1.46718Å). There is also a smaller signal at 2θ = 63.509° corresponding to the Cu Kα2 line and the (400) spacing of InP. Shown in Fig. 2.18 is a X-ray rocking curve for a 1 µm InGaAs epilayer on InP. We have found that the signal from 1 µm thick epilayers is sufficient to distinguish signal peaks from those due to the InP substrate. Due to variations in mounting the sample in the diffractometer, the signal peaks may not be at their expected locations. For example, a slightly misoriented InP sample will not generate signal peaks at 2θ = 63.335° and 2θ = 63.509, corresponding to the Cu Kα1 and Cu Kα2 lines, respectively. However, if we make the assumption that the largest signal is due to the InP Cu Kα1 peak, then the InP Cu Kα2 peak can be readily identified since their separation is known to be 63.509° - 63.335° = 0.1744°. Further, of the

remaining peaks, the largest one is assumed to be that of the epilayer's Cu Kα1 line. Once the peaks have been assigned, the mismatch is given by:

$$\frac{\Delta a}{a_o} = \frac{0.525}{\sin\left(31.667^\circ + \Delta(2\theta)/2\right)} - 1 \qquad (2.8)$$

where Δ2θ is the 2θ separation between the InP and InGaAs Cu Kα1 lines. Taking Δ2θ = 0.1° from Fig. 2.20, $\Delta a/a_o$ is approximately -1.4×10^{-3}. This indicates that the InGaAs epilayer is slightly gallium rich since its lattice constant is larger than that of the InP substrate.

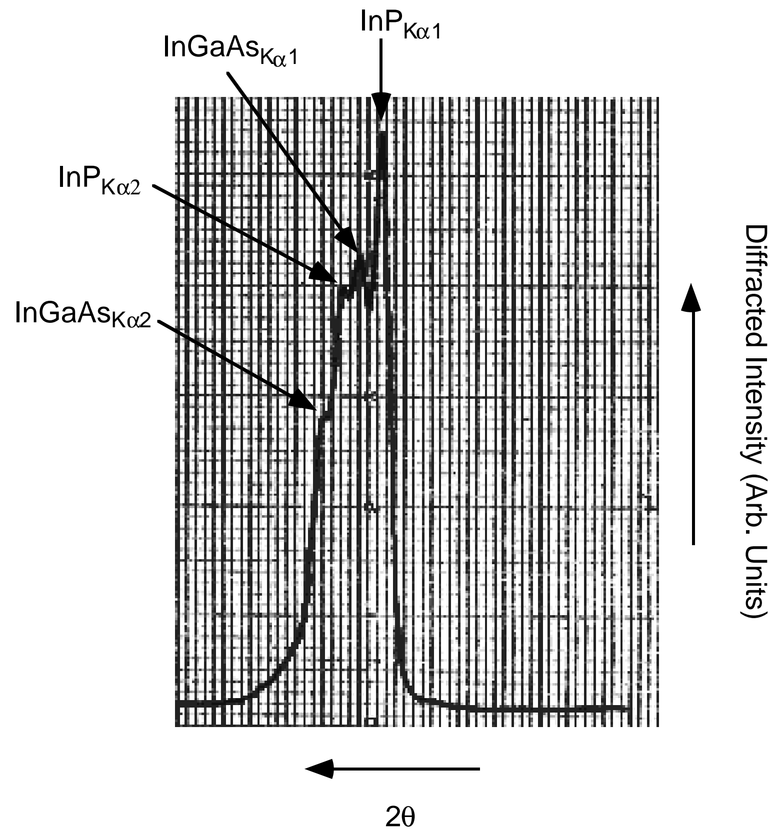

Fig. 2.18 Single crystal X-ray rocking curve of a 1 μm InGaAs epilayer on InP (MBE#2470). The X-ray rocking curve was taken by the author.

As evident in the above discussion, two assumptions must be made for the peak assignment. First, the InP Kα1 and Kα2 lines should be clearly identifiable. Second, the epilayer peaks should not be buried in the InP signal. Furthermore, the resolution of the diffractometer plotter limits the angular resolution to 0.1° 2θ. All these factors combine to limit the mismatch resolution of the SCXRD system to approximately 1×10^{-3}.

Further enhancement in mismatch resolution require the use of a double crystal X-ray diffraction (DCXRD) system. The DCXRD geometry is shown in the bottom half of Fig. 2.17 with the reference InP crystal and the sample parallel to each other. The reference crystal acts as a filter for the incident X-ray radiation and narrows its spectral width. With a slit (not shown in the figure) placed between the reference crystal and sample, the Kα2 line can be blocked, thereby eliminating confusion regarding peak assignment. Therefore, the detector will only record the InP and InGaAs epilayer Kα1 peaks. The DCXRD technique removes many ambiguities inherent in the SCXRD system. A DCXRD rocking curve for the sample MBE#2470 is shown in Fig. 2.19.

Due to an error in the calibration process, the curve is zeroed about the InGaAs peak rather than the InP peak. Nevertheless, the InGaAs lattice mismatch can be readily calculated to be -1.37×10^{-3} with a FWHM width 38 arcseconds. This is surprisingly close to the SCXRD estimate of -1.4×10^{-3}. However, no assumptions regarding peak assignments were required with DCXRD plot. Also, the much higher angular resolution available with the DCXRD system is necessary for mismatch detection below 1×10^{-3}. The mismatch present in our lattice matched InAlGaAs devices ranges from 3×10^{-3} to 5×10^{-4}. The best epilayers have mismatches of approximately 5×10^{-4}. For DBRTD and HBV applications, a mismatch of 3×10^{-3} is easily tolerable.

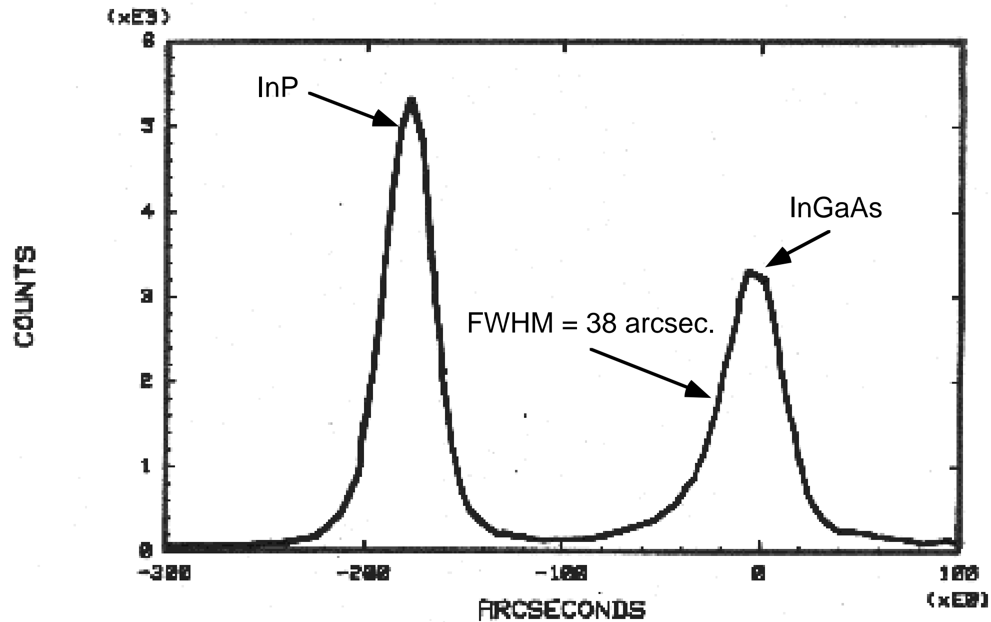

Fig. 2.19 DCXRD Rocking Curve of MBE#2470. The InGaAs lattice mismatch is -1.37×10^{-3}. The DCXRD system belongs to Prof. Russ Dupuis, Dept. of Electrical Engineering, Univ. of Texas at Austin. The X-Ray rocking curve was taken by the author.

2.7.3 Hall Mobility and Photoluminescence

Designing DBRTDs and HBV diodes requires knowledge of the background carrier concentration to determine the electric field profile in the device. As will be discussed in Chapter 4, the electric field determines layer depletion and significantly affects the I - V characteristic. Hall-effect mobility measurements can quickly measure the carrier concentration and also determine the dopant compensation present in the epilayer. Typical carrier mobilities and background carrier concentrations for nominally undoped lattice matched InGaAs samples range from 4000 cm^2/V-s to 7000 cm^2/V-s and 2×10^{15} cm^{-3} to 1×10^{16} cm^{-3} (n-type), respectively. The carrier concentrations and type are typical of

nominally undoped MBE grown InGaAs epilayers. The relatively low mobilities indicate some degree of compensation occurring. Possible sources of unintentional impurities are impurities in the indium source (silicon), insufficient thermal cleaning of the InP substrate [63], out diffusion of impurities from the InP substrate [64]. However, from a device application standpoint, no detrimental effects on DBRTD and HBV performance were noticed due to the relatively low mobility material. Also, high speed $In_{0.52}Al_{0.48}As/In_{0.53}Ga_{0.47}As$ heterojunction bipolar transistors grown in our MBE system have shown state-of-the-art characteristics [65] and apparently have not suffered from the lower mobility material.

Another measure of an epilayer's material quality is given by its PL spectra. With PL one can detect minute impurity concentrations by comparing the measured spectra to known calibrations samples. Shown in Fig. 2.20 is a PL plot of a nominally undoped 2.1 μm InGaAs epilayer (MBE#1785). The peak energy and FWHM at 4.2°K are 0.792 eV and 6 meV, respectively. The peak energy is close to what is expected for lattice matched InGaAs and the FWHM is comparable to the state-of-the-art . The peak transition is due to a donor-to-valence band transition and the lower energy tail is probably due to donor-to-acceptor transitions [66].

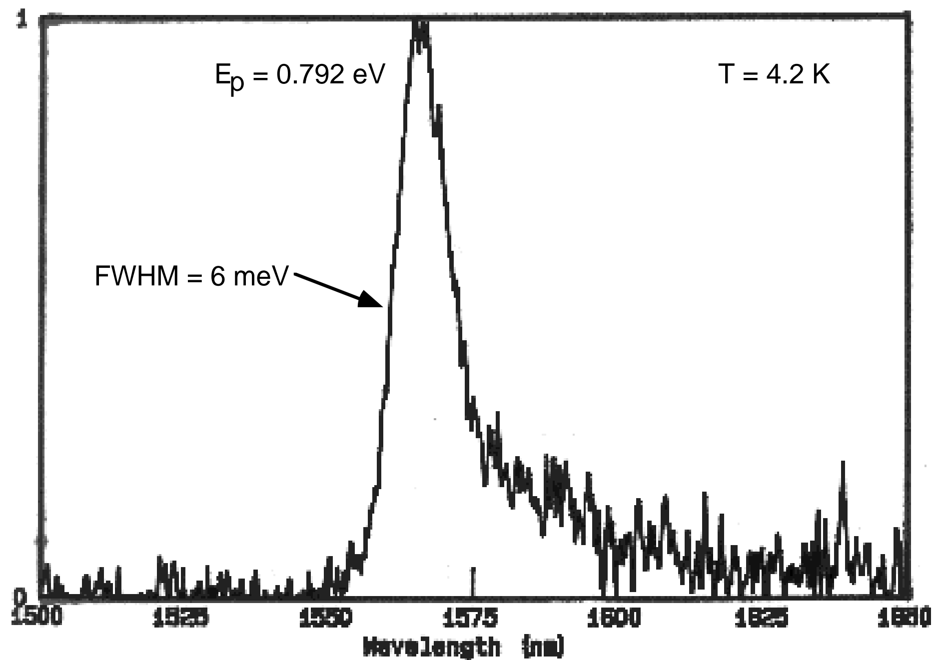

Fig. 2.20 PL spectrum of a 2.1 μm nominally undoped InGaAs film grown on InP (MBE#1785). The peak transition energy and FWHM at T=4.2K is 0.792 eV and 6 meV, respectively. PL spectrum provided by Anand Srinivasan.

2.8 Summary

We have discussed the various steps required to optimize the MBE growth conditions for high performance double barrier resonant tunneling diodes. The RHEED technique was shown to be extremely useful for growth conditions optimization and calibration of growth rates and vital to fabricating reproducible devices. The influence of growth interruptions on the I-V characteristics of AlAs/GaAs DBRTDs was studied and the interrupt schedules were determined by

independent RHEED measurements during prototypical device growth sequences. Our data suggest that interface roughness at inverted and normal interfaces does not play a significant role in determining the transport characteristics of high current density AlAs/GaAs DBRTDs. To further improve device performance, the MBE growth of InAlGaAs based devices grown on InP was investigated. The techniques required to grow lattice matched InGaAs and strained AlAs on InP were discussed. These layers were characterized by Nomarski optical microscopy, X-Ray crystal diffraction, Hall-effect measurements, and photoluminescence.

References

[1] Gerald B. Stringfellow, " Organometallic vapor-phase epitaxy: Theory and Practice", Academic Press, Boston, 1989.

[2] H. Tews, R. D. Schnell, and R. Neumann, " Nonequivalent heterointerfaces in AlGaAs/GaAs double barrier resonant tunneliing diodes grown by metalorganic vapour phase epitaxy," Electronics Lett., vol. 25, No. 25, pp. 1709-1711, 1989.

[3] C. I. Huang, M. J. Paulus, C. A. Bozada, S. C. Dudley, K. R. Evans, C. E. Stutz, R. L. Jones, and M. E. Cheney, Appl. Phys. Lett., vol. 51, No. 2, pp. 121-123, 1987.

[4] H. Tews, " Photoluminescence study of double barrier resonant tunneling diodes grown by metalorganic vapour phase epitaxy," Superlattices and Microstructures, vol. 8, No. 4, pp. 467-474, 1990.

[5] A. C. Gossard, " Growth of Microstructures by Molecular Beam Epitaxy," IEEE Journal of Quantum Electronics, vol. QE-22, No. 9, pp. 1649-1655, 1986.

[6] E. H. C. Parker, Ed., " Technology and Physics of Molecular Beam Epitaxy," New York, Plenum, 1985.

[7] T.J. Mattord, V. P. Kesan, G. E. Crook, T. R. Block, A. C. Campbell, D. P. Neikirk, and B. G. Streetman, " Baffle-free refractory dimer arsenic source for molecular beam epitaxy," J. Vac. Sci. Tech., B 6(6), p. 1667-1670, 1988.

[8] T. J. Mattord, K. Sadra, A. Srinivasan, A. Tang, T. R. Block, Y. C. Albert Shih, D. P. Neikirk, and B. G. Streetman, " Real-time Flux Monitoring and Feedback Control of a Valved Arsenic Source," J. Vac. Sci. Tech. B, vol. 11, No. 3, pp.1050-1052, 1993.

[9] V. Swaminathan and A. T. Macrander," Materials Aspects of GaAs and InP Based Structures," Prentice Hall, Englewood Cliffs, New Jersey, 1991.

[10] F. W. Smith, A. R. Calawa, C. L. Chen, M. J. Manfra, and L. J. Mahoney, " New MBE Buffer Used to Eliminate Backgating in GaAs MESFET's," IEEE Electron Device Lett., vol. 9, No. 2, pp.77-80, 1988.

[11] E. A. Wood, " Vocabulary of Surface Crystallography," J. Appl. Phys., vol. 35, No. 4, pp. 1306-1312, 1964.

[12] J. Zhang, J. H. Neave, P. J. Dobson, and B. A. Joyce, " Effect of diffraction conditions and processes on RHEED intensity oscillations during the MBE growth of GaAs," Appl. Phys. A, pp.317-326, 1987.

[13] E. H. C. Parker, Ed., " Technology and Physics of Molecular Beam Epitaxy,"

New York, Plenum, 1985.

[14] B. F. Lewis, R. Fernandez, A. Madhukar, and F. J. Grunather, " Arsenic-induced intensity oscillations in reflection high-energy electron diffraction measurements," J. Vac. Sci. Tech. B4, No. 2, pp. 560-563, 1986.

[15] Vijay Reddy, " Master's Thesis: Molecular Beam Epitaxial Growth of AlAs/GaAs Double Barrier Resonant Tunneling Diodes," University of Texas at Austin, 1990.

[16] E. H. C. Parker, Ed., " Technology and Physics of Molecular Beam Epitaxy," New York, Plenum, 1985.

[17] A. C. Campbell, V. P. Kesan, T. R. Block, G.E. Crook, D. P. Neikirk, and B. G. Streetman, " Influence ofMBE Growth Temperature on GaAs/AlAs Resonant Tunneling Structures," Journal of Electronic Materials, vol. 18, No. 5, pp. 585-588, 1989.

[18] P. Cheng and J. S. Harris, " Effect of Si doping in AlAs barrier layers of AlAs-GaAs-AlAs double-barrier resonant tunneling diodes," Appl. Phys. Lett., bol. 55, No. 6, pp. 572-574, 1989.

[19] T. J. Rogers, " Ph.D Dissertation: MBE Grown Microcavities for Optoelectronic Devices," University of Texas at Austin, 1992.

[20] D. G. Liu, C. P. Lee, K. H. Chang, J. S. Wu, and D. C. Liou, " Behavior of the first layer growth in GaAs molecular beam epitaxy," Appl. Phys. Lett., vol. 57, No. 14, pp. 1392-1394, 1990.

[21] V. K. Reddy, A. J. Tsao, and D. P. Neikirk, " High Peak-to-Valley Current Ratio AlGaAs/AlAs/GaAs Double Barrier Resonant Tunneling Diodes," Electronics Lett., vol. 26, No. 21, pp.1742-1744, 1990.

[22] A. Madhukar, T. C. Lee, M. Y. Yen, P. Chen, J. Y. Kim, S. V. Ghaisas, and P. G. Newman, " Role of surface kinetics and interrupted growth during molecular beam epitaxial growth of normal and inverted GaAs/AlGaAs (100) interfaces: A reflection high-energy electron diffraction intensity dynamics study," Appl. phys. Lett., vol. 46, No. 12, pp. 1148-1150, 1985.

[23] B. A. Joyce, J. Zhang, J. H. Neave, and P. J. Dobson, " The Application of RHEED Intensity Effects to Interrupted Growth and Interface Formation During MBE Growth of GaAs/AlGaAs Structures," Appl. Phys. A, vol. 45, pp. 255-260, 1988.

[24] M. Tanaka and H. Sakaki, " Atomistic Models of Interface structures of GaAs-$Al_xGa_{1-x}As$ (x= 0.2-1) quantum wells grown by interrupted and uninterrupted

MBE," Journal of Crystal Growth, vol. 81, pp. 153-158, 1987.

[25] Masaaki Tanaka, Hiroyuki Sakaki, and Junji Yoshino, " Atomic-scale structures of top and bottom heterointerfaces in GaAs-$Al_xGa_{1-x}As$ (x=0.2-1) quantum wells prepared by molecular beam epitaxy with growth interruption," JJAP, vol. 25, No. 2, pp.L155-L158, 1986.

[26] D. S. Katzer, D. Gammon, and B. V. Shanabrook, " Modification of the Microroughness of MBE Grown GaAs/AlAs Interfaces through Changes in the Growth Temperature.

[27] L. N. Pfeiffer, K. W. West, and H. L. Stormer, " Electron mobilities exceeding 10^7 cm^2/V-s in modulation-doped GaAs," Appl. Phys. Lett., vol. 55, 1989.

[28] P. Gueret and C. Rossel, " Investigations on resonant tunneling and the role on interface roughness scattering in quantum wells," in Resonant Tunneling in Semiconductors, Editied by L. L. Chang et al., Plenum Press, New York, 1991.

[29] Private communication with P. Gueret, IBM Zurich, Oct. 1991.

[30] M. Lentzen, D. Gerthsen, A. Forster, and K. Urban, " Growth mode and strain relaxation during the initial stage of $In_xGa_{1-x}As$ growth on GaAs (001)," Appl. Phys. Lett., vol. 60, No. 1, pp. 74-77, 1992.

[31] J. Zhang, J. H. Neave, P. J. Dobson, and B. A. Joyce, " Effects of Diffraction conditions and Processes on RHEED Intensity Oscillations During the MBE Growth of GaAs," Appl. Phys. A., No. 42, pp. 317-326, 1987.

[32] V. K. Reddy and Dean P. Neikirk, " Influence of growth interruption on I-V characteristics of AlAs/GaAs double barrier resonant tunneling diodes," J. Vac. Sci. Tech. B, vol. 10, No. 2, pp.1045-1047, 1992.

[33] John D. Bruno and J. S. Hurley, " Effect of interface roughness on the current-voltage characteristic of a resonant tunneling diode," Superlattices and Microstructures, vol. 11, No. 1, pp. 23-26, 1992.

[34] D. Z.-Y. Ting, S. K. Kirby, and T. C. McGill, " Three-dimensional simulations of quantum transport in semiconductor nanostructures," J. Vac. Sci. Tech. B, vol. 11, No. 4, pp. 1738-1742, 1993.

[35] James Leo and A. H. MacDonald, " Disorder-Assisted Tunneling through a Double-Barrier Structure," Phys. Rev. Lett., vol. 64, No. 8, pp.817-820, 1990.

[36] A. J. Tsao, V. K. Reddy, D. R. Miller, K. K. Gullapalli, and D. P. Neikirk, " Effect of barrier thickness asymmetries on the electrical characteristics of AlAs/GaAs double barrier resonant tunneling diodes," J. Vac. Sci. Tech. B, 1992.

[37] Wai Lee and Clifton G. Fonstad, " The growth of high mobility InGaAs and InAlAs layers by molecular beam epitaxy," J. Vac. Sci. Technol. B 4, No. 2, pp. 536-538, 1986.

[38] V. Swaminathan, R. A. Stall, A. T. Macrander, and R. J. Wunder, " Photoluminescence characterization of molecular beam epitaxy grown $In_xGa_{1-x}As$ ($0.51 < x < 0.57$)," J. Vac. Sci. Technol. B 3, No. 6, pp. 1631-1636, 1985.

[39] Hideho Saito, John O. Borland, Hajime Asahi, Haruo Nagai, and Kiyoshi Nawata, " Hillock Defects in InGaAs/InP Multi-Layers Grown By MBE," Journal of Crystal Growth, vol. 64, pp. 521-528, 1983.

[40] G. J. Davies, R. Heckingbottom, H. Ohno, C. E. C. Wood, and A. R. Calawa, " Arsenic stabilization of InP substrates for growth of $Ga_xIn_{1-x}As$ layers by molecular beam epitaxy," Appl. Phys. Lett., vol. 37, No. 3, pp. 290-293, 1980.

[41] J. P. Praseuth, M. C. Joncour, J. M. Gerard, P. Henoc, and M. Quillec, " Growth and characterization of AlGaInAs lattice matched to InP grown by molecular beam epitaxy," J. Appl. Phys., vol. 63, No. 2, pp. 400-403, 1988.

[42] J. Massies, F. Turco, A. Saletes, and J. P. Contour, " Experimental evidence of difference in surface and bulk compositions of $Al_xGa_{1-x}As$, $Al_xIn_{1-x}As$, and $Ga_xIn_{1-x}As$ Epitaxial layers grown by molecular beam epitaxy," Journal of Crystal Growth, vol. 80, pp.307-314, 1987.

[43] R. Wunder, R. Stall, R. Malik, and S. Woefler, " Automated growth of $Al_xGa_{1-x}As$ and $In_xGa_{1-x}As$ by molecular beam epitaxy using an ion gauge flux monitor," J. Vac.Sci. Technol. B 3 (4), pp. 964-967, 1985.

[44] Minimum order of $2000 for 6 square inches of InAs. The supplier is a Russian company and the epi surface quality is unknown.

[45] Paul R. Berger, Kevin Chang, Pallab Bhattacharya, and Jasprit Singh, " Role of strain and growth conditionson the growth front profile on $In_xGa_{1-x}As$ on GaAs during the pseudomorphic growth regime," Appl. Phys. Lett., vol. 53, No. 8, pp.684-686, 1988.

[46] J. W. Matthews and A. E. Blakeslee, " Defects in Epitaxial Multilayers: I. Misfit Dislocations," J. of Crystal Growth, vol. 27, pp. 118-125, 1974.

[47] Sadao Adachi, " GaAs, AlAs, and $Al_xGa_{1-x}As$: Material parameters for use in research and device applications," J. Appl. Phys., vol. 58, No.3, pp. R1-R29, 1985.

[48] J. H. Van der Merwe, " Crystal interfaces: Part I, Semi-infinite crystals," J. Appl. Phys., vol. 34, No. 1, pp. 117-122, 1963.

[49] J. W. Matthews and A. E. Blakeslee, " Defects in Epitaxial Multilayers: III. Preparation of almost perfect layers," J. of Crystal Growth, vol. 32, pp. 265-273, 1976.

[50] I. J. Fritz, P. L. Gourley, and L. R. Dawson, " Critical layer thickness in $In_{0.2}Ga_{0.8}As/GaAs$ single strained quantum well structures," Appl. Phys. Lett., vol. 51, No. 13, pp. 1004-1006, 1987.

[51] J. P. Reithmaier, H. Cerva, and R. Losch, " Investigation of the critical layer thickness in elastically strained InGaAs/GaAlAs quantum wells by photoluminescence and transmission electron microscopy," Appl. Phys. Lett., vol.54, No. 1, pp. 48-50, 1989.

[52] H. Temkin, D. G. Gershoni, s. N. G. Chu, J. M. Vandenberg, R. A. Hamm, and M. B. Panish, " Critical layer thickness in strained Ga1-xInxAs/InP quantum wells," Appl. Phys. Lett., vol. 55, No. 16, pp. 1668-1670, 1989.

[53] I. J. Fritz, S. T. Picraux, L. R. Dawson, T. J. Drummond, W. D. Laidig, and N. G. Anderson, " Dependence of critical layer thickness on strain for $In_xGa_{1-x}As/GaAs$ strained-layer superlattices," Appl. Phys. Lett., vol. 46, No. 10, pp. 967-968, 1985.

[54] M. J. Ekenstedt, S. M. Wang, and T. G. Anderson, " Temperature-dependent critical layer thickness for $In_{0.36}Ga_{0.64}As/GaAs$ single quantum wells," Appl. Phys. Lett., vol. 58, No. 8, pp. 854-855, 1991.

[55] F. G. Celii, Y. C. Kao, H. Y. Liu, L. A. Files-Sessler, and E. A. Beam III, " Laser light scattering detection of InGaAs strained layer relaxation during molecular-beam epitaxial growth," J. Vac. Sci. Tech. B, vol. 11, No. 3, pp.1014-1017, 1993.

[56] F. G. Celii, Y. C. Kao, E. A. Beam III, and L. A. Files-Sessler, " In situ determination of critical layer thickness of AlAs/InGaAs/InAs resonant tunneling structures on InP using laser light scattering," Presented at 1993 Electronic Materials Conference, Santa Barbara, CA, 1993.

[57] D. M. Hwang, S. A. Schwartz, T. S. Ravi, R. Bhat, and C. Y. Chen, " Strained-Layer Relaxation in fcc Structures via the Generation of Partial Dislocations," Phys. Rev. Lett., vol. 66, No. 6, pp.739-742, 1991.

[58] S. M. Sze, ed., " VLSI Technology", S. M. Sze, ed., McGraw Hill, Singapore, 1983.

[59] Private communication with F. Celii of Texas Instruments, October 1993.

[60] P. Franzoni, G. Salviati, F. Genova, A. Stano, and F. Taiariol, " Misfit dislocations in InGaAs/InP MBE Single Heterostructures," Journal of Crystal

Growth, vol. 75, pp. 521-534, 1986.

[61] S. Kalem, " Molecular-beam epitaxial growth and transport properties of InAs epilayers," J. Appl. Phys., vol. 66, No. 1, pp.3097-3103, 1989.

[62] V. Swaminathan and A. T. Macrander, " Materials Aspects of GaAs and InP Based Structures," Prentice Hall, Englewood Cliffs, New Jersey, 1991.

[63] T. Mishima, M. Takahama, Y. Uchida, T. Tanoue, and S. Takahashi, " Very high purity $In_{0.53}Ga_{0.47}As$ grown by molecular beam epitaxay," Journal of Electronic Materials, vol. 20, No. 1, pp. 113116, 1991.

[64] A. S. Brown, S. C. Palmateer, G. W. Wicks, L. F. Eastman, and A. R. Calawa, " The behavior of unintentional impurities in $Ga_{0.47}In_{0.53}As$ grown by MBE," Journal of Electronic Materials, vol. 14, No. 3, pp.367-378, 1985.

[65] C. Kyono, V. Reddy, S. Binari, and D. Neikirk, unpublished.

[66] V. Swaminathan, R. A. Stall, A. T. Macrander, and R. J. Wunder, " Photoluminescence characterization of molecular beam epitaxy grown $In_xGa_{1-x}As$ $(0.51<x<0.57)$," J. Vac. Sci. Tech. B, vol. 3, No. 6, pp. 1631-1636, 1985.